Temporal integration and 1/f power scaling in a circuit model of cerebellar interneurons

Reinoud Maex[1] and Boris Gutkin[1,2]

[1]Department of Cognitive Sciences, École Normale Supérieure, PSL Research University, Paris, France

[2]Centre for Cognition & Decision Making, Higher School of Economics, Moscow, Russian Federation

Corresponding author: Reinoud Maex
Department of Cognitive Sciences
École Normale Supérieure
29 rue d'Ulm
Paris 75005
France
Phone: +33 1 44 32 27 98
Email: reinoud.maex@ens.fr

Running head: Temporal integration in an inhibitory circuit

Contents: 57 pages, 10 figures, 2 tables
Words: 14,344 (total), 227 (abstract), 582 (introduction), 2,721 (discussion)

Abstract

Inhibitory interneurons interconnected via electrical and chemical ($GABA_A$ receptor) synapses form extensive circuits in several brain regions. They are thought to be involved in timing and synchronization through fast feed-forward control of principal neurons. Theoretical studies have shown, however, that whereas self-inhibition does indeed reduce response duration, lateral inhibition, in contrast, may generate slow response components through a process of gradual disinhibition. Here we simulated a circuit of interneurons (stellate and basket cells) of the molecular layer of the cerebellar cortex, and observed circuit time-constants that could rise, depending on the parameter values, to more than one second. The integration time scaled both with the strength of inhibition, vanishing completely when inhibition was blocked, and with the average connection distance, which determined the balance between lateral and self-inhibition. Electrical synapses could further enhance the integration time by limiting heterogeneity among the interneurons, and by introducing a slow capacitive current. The model can explain several observations, such as the slow time-course of OFF-beam inhibition, the phase lag of interneurons during vestibular rotation, or the phase lead of Purkinje cells. Interestingly, the interneuron spike trains displayed power that scaled approximately as *1/f* at low frequencies. In conclusion, stellate and basket cells in cerebellar cortex, and interneuron circuits in general, may not only provide fast inhibition to principal cells, but also act as temporal integrators that build a very-short-term memory.

New & noteworthy

The most common function attributed to inhibitory interneurons is feed-forward control of principal neurons. In many brain regions, however, the interneurons are densely interconnected via both chemical and electrical synapses, but the function of this coupling is largely unknown. Based on large-scale simulations of an interneuron circuit of cerebellar cortex, we propose that this coupling enhances the integration time-constant, and hence the memory trace, of the circuit.

Keywords: cerebellum, computational model, lateral inhibition, stellate cell, basket cell, integrator

Glossary: $GABA_AR$, GABA type-A receptor; MLI, molecular-layer interneuron; PC, Purkinje cell; PF, parallel fiber; CV, coefficient of variation.

Introduction

Even though the cerebellar cortex possesses an extremely fast microcircuit, with sensory inputs arriving before they reach the thalamus, it also implements functions (such as motor control, sensory cancellation, and delay conditioning) that require a short-term memory (Mauk and Buonomano 2004). The unique capacity of cerebellar cortex to adapt its timing, which can be lost when the circuit is genetically modified (Wulff et al. 2009), indicates that this short-term memory must reside at least temporarily within the cerebellar cortex itself, although it may be consolidated in

other structures such as the cerebellar nuclei and brainstem (Longley and Yeo 2014). In the absence of overt feedback excitation, candidate mechanisms for memory traces are slow synaptic transmission via metabotropic receptors (Johansson et al. 2015), intrinsic neuronal membrane properties, and lateral inhibition.

A previous modeling study (Maex and Steuber 2013) predicted that if the principal neurons or Purkinje cells (PCs) were connected through lateral inhibition, a premise that has recently been validated (Witter et al. 2016), they could build memory traces lasting up to 15 seconds, at least at low spike frequencies. It is well known, however, that PCs do not always lag, but often lead, their presumed input from the excitatory parallel fibers (PFs) (Miles et al. 1980; De Zeeuw et al. 1995; Lisberger 2009). As such, the cerebellar cortex has been suggested to act as an adaptive lead-lag compensator (Fujita 1982).

We here study temporal pre-processing within the circuit of inhibitory interneurons of the molecular layer (stellate and basket cells, jointly called molecular-layer interneurons or MLIs). Like several classes of neocortical interneurons (Galarreta and Hestrin 1999; Gibson et al. 1999), MLIs are densely interconnected both via chemical $GABA_A$ receptor ($GABA_AR$) and electrical synapses (Llano and Gerschenfeld 1993; Mann-Metzer and Yarom 1999; Rieubland et al. 2014).

In a theoretical study, Cannon et al. (1983), inspired by Morishita and Yajima (1972), showed that properly laid lateral inhibition may enhance the circuit time-constant by several orders of magnitude. In brief, whereas self-inhibition ('self' referring not only to autapses but also to reciprocal synapses between neurons sharing common inputs) accelerates response transients and decreases the circuit time-constant, lateral inhibition ('lateral' referring to reciprocal inhibition between neurons with non-shared inputs) prolongs the response duration and increases the time-

constant. Hence, an inhibitory circuit transmits common inputs with a fast time-constant, whereas differences in input are temporally integrated with a time-constant that increases with the strength of reciprocal inhibition.

To appreciate the computational power of this mechanism, consider in Fig. 1 the responses of two reciprocally connected inhibitory neurons, modeled here as half-wave-rectified leaky integrators with an intrinsic time-constant of 20 ms. The pair of neurons responds immediately to a shared rectangular input applied from 20 to 80 s, irrespective of the strength of inhibition. In sharp contrast, the response to a non-shared input, presented in a push-pull fashion from 40 to 60 s, shows a much slower time-course. With the strength of inhibition set at 0.99 (bottom left), the response time-constant rises to 2 s. At still stronger inhibition (0.999, bottom right), the integration time even rises to 20 s but in this case integration is never completed because the pair becomes functionally disconnected once the activity of the weaker neuron falls below threshold.

--- Figure 1 about here ---

Hence non-linear components (the spike threshold) and phenomena (a winner-take-all dynamics) make it difficult to predict the degree of integration in actual interneuron circuits. We therefore built a detailed computational model of the cerebellar MLI circuit and conducted simulations to calculate its presumed integration time.

Materials and Methods

We built a biophysically detailed circuit of the interneurons of the molecular layer of the cerebellar cortex, intended to replicate in vivo findings (at 37 °C), and using

124 reported data from juvenile or adult rats, occasionally from mice, cats and the guinea
125 pig.
126
127 *The multi-compartmental MLI model: morphology and passive properties.* The
128 present study does not distinguish between stellate and basket cells, assuming they
129 form a single population of MLIs (Eccles et al. 1966; Midtgaard 1992; Häusser and
130 Clark 1997; Sultan and Bower 1998; Rieubland et al. 2014). The difference in their
131 axonal length (Chan-Palay and Palay 1972), or mean connection distance, was a free
132 parameter that is studied separately in Fig. 6*A*.
133 --- Figure 2 about here ---
134 The model MLIs had three passive dendrites each branching twice, giving 21
135 compartments in total (3 primary, 6 secondary and 12 tertiary) (Fig. 2*A*). Each
136 dendritic compartment was a cylinder of 30 μm length and 0.4 μm diameter, as in
137 Abrahamsson et al. (2012). The spherical soma was 12.5 μm in diameter, which is
138 larger than the 7-10 μm commonly reported (Llano and Gerschenfeld 1993; Kondo
139 and Marty 1998; Molineux et al. 2005; Abrahamsson et al. 2012) but needed to
140 compensate for the absence of an axon. Indeed, the axons of actual MLIs contribute
141 considerably to the whole-cell capacitance (up to 65% for basket cells in Alcami and
142 Marty (2013)), but incorporating them in circuit models is impracticable. With a
143 specific membrane capacitance C_M of 1 μF cm^{-2} the total capacitance of an isolated
144 model MLI (not electrically coupled in a circuit) measured 12.83 pF, as compared to
145 8-14.7 pF for actual rat stellate and basket cells (Alcami and Marty 2013). The
146 specific axial and membrane resistance were set at R_A = 100 Ω cm and R_M = 30.3 kΩ
147 cm^2.
148

149 *The MLI dendrite: gap junction coupling.* Electrical synapses were made on four
150 secondary and four tertiary dendritic compartments (black dots in Fig. 2*A*). They had
151 a (voltage-independent, non-rectifying) conductance of 200 pS, as compared to 93
152 and 210 pS for stellate and basket cells in 12-17 day old rats (Alcami and Marty
153 2013), and 4.25 GΩ in P7-P17 guinea pigs (Mann-Metzer and Yarom 1999).
154
155 *The MLI soma: voltage-gated channels.* In addition to the spike-generating fast
156 sodium channel (NaF) and the delayed-rectifier potassium channel (KDr), actual
157 MLIs have a high-voltage-activated L-type Ca channel (CaL) (Collin et al. 2009;
158 Anderson et al. 2010; Liu et al. 2011), a low-voltage-activated T-type Ca channel
159 (CaT) (Molineux et al. 2005), an inactivating A-type K channel (KA) (Mann-Metzer
160 and Yarom 2000; Molineux et al. 2005), a BK-type Ca-activated K channel (BK) (Liu
161 et al. 2011), and a hyperpolarization-activated channel generating the mixed-cationic
162 h-current (Mann-Metzer and Yarom 2002a; Molineux et al. 2005; Mejia-Gervacio and
163 Marty 2006; Carzoli and Liu 2015). Models for these channels were taken from the
164 GENESIS libraries of Golgi and Purkinje cells, except for two modifications discussed
165 below. We mention for completeness that the channel implementations were based on
166 Gabbiani et al. (1994) (InNa, KDr, CaL and h), Hirano and Hagiwara (1989) and
167 Kaneda et al. (1990) (CaT), Bardoni and Belluzzi (1993) (KA), and Moczydlowski
168 and Latorre (1983) (BK).
169 A first modification concerned the Ca^{2+} dynamics, which was taken much
170 faster than in the Golgi cell model by Maex and De Schutter (1998), where a 200 ms
171 decay time-constant was used to implement the slow spike-rate adaptation of actual
172 Golgi cells (Dieudonné 1998). Although spike-rate adaptation has been reported for
173 MLIs (Midtgaard 1992; Witter and De Zeeuw 2015), an acceleration of spikes was

also observed (see Fig. 1*B* of Mann-Metzer and Yarom (2000) and Fig. 1*C* of Jörntell and Ekerot (2003)). We therefore reduced the decay time-constant of the free-Ca^{2+} pool from 200 to 2 ms, and increased by a factor of 100 the density of the BK channels to compensate for the resulting reduction of available Ca^{2+}.

The second modification concerned the CaT and KA channels, which were tuned to reproduce the characteristic rebound spiking of MLIs (Molineux et al. 2005). To this end, the gates of the KA and CaT channels were repositioned on the voltage axis. More particularly, the rate constants of the inactivation gate of the CaT channel were shifted by +10 mV to the right, centering half-maximal inactivation and activation at -83 and -44 mV, respectively. Likewise, all rate-constants of the KA channel were shifted by +8 mV, centering these curves at -79 and -46 mV.

The peak conductances of the voltage-gated channels were set as follows (in mS cm^{-2}): NaF 80.0; KDr 13.6; CaL 0.83; CaT, 0.4; KA 5.2; BK 57.2 and h 0.04. The reversal potential of the leak current was drawn from a uniform distribution between -54 and -52 mV. Taken together, this conferred on the population of MLIs a resting spike rate of 7.95 ± 3.84 s^{-1} (range 0–13.74 s^{-1}, 35 of 800 MLIs (4.4%) being silent at rest). Some circuit simulations were run with MLIs lacking the CaT channel (see Fig. 6*A*). The parameters were set as above except for the KA peak conductance of 0.52 mS cm^{-2}. These circuits produced results that were qualitatively indistinguishable, but they had slightly lower integration times.

MLI responses to current injection. In response to -10 pA current injection, the *isolated* model MLI hyperpolarized from a holding potential of -66.4 mV to a plateau at -77.7 mV, yielding an input resistance of 1.128 GΩ (Fig. 2*B*). The time-constant (time to 1/*e* peak response) measured 19.7 ms. Notice also the sag in the response,

199 caused by strong activation of the h-current below its half-maximal-activation voltage
200 of -75 mV. When the same MLI was part of an electrically coupled circuit (MLI 233
201 in Fig. 2*C*), its input resistance decreased to 573 MΩ with a concomitant decrease in
202 time-constant to 5.84 ms. These values, calculated in the absence of synaptic input, lie
203 between those of actual MLIs recorded in vitro (643 MΩ and 13.1 ms in Häusser and
204 Clark (1997)) and in vivo (139 MΩ and 2.4 ms in Jörntell and Ekerot (2003)). MLI
205 238, which was electrically coupled to MLI 233, reached a steady-state
206 hyperpolarization of 6.81 % amplitude, as compared to actual coupling coefficients of
207 7.13 % in P18-P23 rats (Rieubland et al. 2014) and 12 % in P7-P17 guinea pigs
208 (Mann-Metzer and Yarom 1999).

209 As mentioned above, the MLI model reproduced the characteristic rebound
210 spiking observed by Molineux et al. (2005) (Fig. 2*D*). The latency of the first rebound
211 spike increased from 57 ms at a holding potential of -84 mV (Fig. 2*D*, left) to a
212 maximal value of 136 ms at -72 mV (middle) and back to 57 ms at -57 mV (right).
213 Evidently, at -84 mV more than half of the CaT channels were available (de-
214 inactivated) to evoke a fast rebound spike. At -72 mV, the CaT channel was too much
215 inactivated to overcome the damping effect of KA activation, whereas at -57 mV KA
216 itself was inactivated for more than 90%. Notice also the absence of spike-rate
217 adaptation in the present MLI model.

218

219 *The MLI model: synaptic channels.* Because the circuit dynamics described in the
220 present study did not depend on the precise manner the MLIs were excited, their
221 excitatory synapses are described only cursorily. The dendritic compartments had
222 AMPAR synapses of 1.8 nS peak conductance, rising and decaying with 0.03 ms and
223 0.5 ms time-constants (Carter and Regehr 2002; Clark and Cull-Candy 2002). The

224 high peak conductance was needed to obtain large somatic EPSPs up to 5.33 mV
225 (Jörntell and Ekerot 2003). Even the most distal synapses evoked EPSPs of 2.91 mV,
226 as in Abrahamsson et al. (2012). During voltage clamp at -70 mV, the EPSCs ranged
227 in amplitude from 27 to 149 pA. The model MLI did not have NMDA receptors,
228 which in actual MLIs are located extrasynaptically and are presumably only activated
229 by very strong PF activity (Clark and Cull-Candy 2002) or by spilled-over glutamate
230 from climbing fiber synapses on adjacent PCs (Szapiro and Barbour 2007; Mathews
231 et al. 2012).

232 The characteristics of the much more important $GABA_AR$ synapse are
233 summarized in Table 1, for both the isolated and electrically coupled MLI. Its
234 conductance rose and decayed with time-constants of 0.1 and 3 ms, respectively,
235 reaching a peak of 2.77 nS, as compared to 1-5 nS in juvenile rats (Zorrilla de San
236 Martin et al. 2015). The IPSCs of *isolated* MLIs varied in amplitude from 15.5 to 55.5
237 pA when the soma was clamped at -50 mV, generating a driving force of 20 mV with
238 respect to the E_{Cl} of -70 mV. These peak currents approximate the 61 to 226 pA
239 obtained in vitro at a three times greater driving force (Llano and Gerschenfeld 1993).
240 When taking into account the relative distribution of the location of synapses (Table
241 1, second column), the mean IPSC amplitude in an isolated MLI measured 22.0 ±
242 10.5 pA.

243 --- Table 1 about here ---

244 When the MLIs were embedded in the electrically coupled circuit, however,
245 the IPSC amplitude dropped to near physiological values, ranging from 9.4 to 20.5 pA
246 for dendritic synapses with the soma-evoked IPSC unchanged at 55.5 pA ('circuit
247 MLI' in Table 1). In order to avoid too great variability in excitability between
248 different MLIs, caused by variation in the number of $GABA_AR$ synapses they

249 received on their soma, the somatic synapses were normalized by dividing their peak
250 conductance by the actual number of synapses received (which varied from 0 to 14).
251 The combined effect of electrical coupling and somatic normalization reduced the
252 average IPSC amplitude to 12.8 pA, which is close to the 11.2 ± 9.2 pA recorded by
253 Rieubland et al. (2014) using a 27.5 mV driving force. A similar decrease in
254 amplitude was observed for the IPSPs (Fig. 2*E*). Electrical coupling also reduced the
255 decay time of IPSPs from 27 to 12 ms.

256 Finally, Fig. 2, *F* and *G,* illustrates MLI activity during the sinusoidal PF
257 stimulation protocol used for Figs. 4-6. Notice that spikelets were too small (0.2 mV)
258 to be observed on the membrane voltage trace of Fig. 2*F* since the action potentials
259 were strongly attenuated during their retrograde and anterograde courses along the
260 very narrow dendrites (see also Fig. 8*C*). Underneath (Fig. 2*G*) is an IPSC trace from
261 the same MLI with its soma voltage-clamped at -50 mV and its PF synapses blocked,
262 the remainder of the circuit being simulated as before. From this, the average
263 $GABA_AR$ current measured 38.5 ± 21.7 pA.

264

265 *The MLI circuit.* We simulated a narrow sagittal strip about the width of a microzone
266 (Dean et al. 2010), comprising a volume of 100 x 720 x 300 μm^3 (PF x sagittal x
267 radial axis). This strip contained 5 x 40 x 4 = 800 MLIs arranged in four horizontal
268 layers, 34.6 μm apart, so that together the dendrites covered the entire depth of the
269 molecular layer (Fig. 3, *A* and *B*). Rows of MLIs with caudally and rostrally
270 projecting axons alternated along the sagittal axis (grey and white cell somata in Fig.
271 3*A*). Within each layer the somata were 40 or 20 μm apart (the latter value being used
272 in the standard model), corresponding to cell densities of about 27,000 and 110,000
273 mm^{-3}, respectively. These values are of the same order of magnitude as the MLI

274 densities estimated for cats (18,695 stellate plus 6,577 basket cells mm^{-3} in Ito (1984),
275 based on Palkovits et al. (1971)), and rats (97,465 MLIs mm^{-3} in Korbo et al. (1993),
276 based on a PC density of 10,100 mm^{-3} and an MLI-PC ratio of 9.65). No qualitative
277 differences were found between circuits of these two densities (see Fig. 6*A*).

278 For the standard circuit, 17,043 PFs were randomly positioned at their virtual T-
279 bifurcations within a volume that comprised the MLI circuit extended on either side
280 by half the PF length of 5 mm. Note that the PFs in the model represented only a
281 fraction of their actual number, given that the present MLI circuit could accommodate
282 along its sagittal axis the dendrites of three to four PCs and that each PC dendrite is
283 thought to be traversed by 400,000 PFs (Ito 1984). Computationally, however, the
284 PFs, modeled as random spike generators, were expensive, and arguably the actual PF
285 activity is clustered and sparse (Wilms and Häusser 2015; but see also Giovannucci et
286 al. 2017).

287

288 *Circuit connectivity: chemical synapses.* The MLIs received on average 32.8 ± 5.95
289 PF synapses. Note again that this number is almost two orders of magnitude less than
290 what actual MLIs would receive as predicted from an intersynaptic distance of 0.7 μm
291 (Abrahamsson et al. 2012) and an average dendritic length of 1,189 μm (Sultan and
292 Bower 1998), but this sparseness can be justified as above.

293 The most important circuit parameter was the spatial kernel of $GABA_AR$-
294 mediated inhibition among MLIs. Its profile determined the number of synapses made
295 by the (virtual) MLI axon, and their sagittal distance from the parent soma (the
296 connection length) (see Figs. 3 and 6 for examples). Sultan and Bower (1998)
297 distinguished a proximal axon plexus centered at 29 μm from the soma and a distal
298 one at 153 μm. We implemented the synaptic connections using two ellipsoid kernels

299 as described in Maex and Steuber (2013). The average bouton distance, which is a
300 critical parameter, could be varied either by changing the centers of the proximal and
301 distal kernels, or their relative weight (their probability of making synapses) (see
302 insets to Fig. 6*A*). For instance, when the weight of the distal plexus, centered here at
303 160 μm from the soma, was increased from 1/3 over 1 to 3, the mean sagittal
304 connection distance, as measured from the afferent soma to the synaptic compartment
305 on the efferent MLI, increased from 80.2 ± 70.3 over 112.4 ± 70.9 to 131.8 ± 65 μm,
306 the latter being the value used in our standard model. As a comparison, in the sample
307 of Sultan and Bower (1998) the mean bouton distance was only 91 μm, but with a
308 great variation among MLIs (standard deviation of the mean of 67 μm), and an even
309 greater variation in axonal spread (from < 100 μm to > 550 μm, mean 266 μm). In
310 the cat, the length of basket cell axons has been reported to vary from 225 to 800 μm
311 (Bishop 1993), and optical imaging in guinea pigs revealed OFF-beam inhibition that
312 extended up to 800 μm from the beam (Cohen and Yarom 2000). Irrespective of
313 distance, the synaptic latency was taken 1.6 ms (Astori et al. 2009; Zorrilla de San
314 Martin et al. 2015).

315 In the standard circuit of 800 MLIs, the above kernels laid connections between
316 26,465 pairs of MLIs, of which 5.6 % were reciprocally connected, as compared to
317 7.8 % in Rieubland et al. (2014). Taken together, each MLI received on average 39.0
318 ± 11.0 $GABA_AR$ synapses from 35.0 ± 9.6 MLIs. This number of $GABA_AR$ synapses
319 is poorly constrained in the literature. In an electron-microscopic study, Lemkey-
320 Johnston and Larramendi (1968) examined 716 synapses on MLIs, 588 (82.1 %) of
321 which were made by PFs and 53 (7.4 %) by MLIs (admittedly their sample was biased
322 toward somatic synapses). Given a presumptive value of 1700 PF synapses (see
323 above), the predicted number of $GABA_AR$ synapses would be 153, which is in

324 agreement with Nusser et al. (1997) who counted 10-fold fewer symmetrical than
325 asymmetrical synapses. This actual number is greater than the 39 synapses used here,
326 but the present model did not allow for synaptic failure, which can amount to 60 % in
327 adult rats (Pouzat and Marty 1998; Pulido et al. 2015). More recently, Briatore et al.
328 (2010) assessed the density of $GABA_AR$ synapses in the molecular layer of a mouse
329 strain in which PCs were devoid of $GABA_ARs$. From the fraction of remaining
330 synapses in their KO mice, they estimated that 30 % of the synapses made by MLIs in
331 wild-type mice innervate other MLIs, implying that an MLI would receive 400
332 $GABA_AR$ synapses. Sultan and Bower (1998), in contrast, counted an average of 149
333 ± 61 boutons along the MLI axon, which would predict the number of synapses on
334 other MLIs to be only 45, but as noted by Briatore et al. (2010) this number may be an
335 underestimate as a single bouton may innervate multiple cells.
336
337 *Circuit connectivity: electrical synapses.* Finally, each MLI in the circuit made 12 gap
338 junctions with the dendritic compartments of neighboring MLIs. Two configurations
339 were tested: in the first, MLIs were coupled via two gap junctions to six neighbors
340 within the same (rostrally versus caudally projecting) subclass; in the second,
341 electrical synapses were made on neighbors of either class. Again, no apparent
342 differences were observed. Alcami and Marty (2013) estimated an average coupling
343 to four neighbors from capacitive measurements, but Mann-Metzer and Yarom (2000)
344 mentioned clusters of up to 9 dye-coupled cells, and Rieubland et al. (2014) found a
345 local connection probability of 0.42. All electrical synapses were made on MLIs with
346 sagittal dendritic planes less than 20 μm apart along the transverse (PF) axis.
347

348 *Stimulation of the MLI circuit.* The circuit received excitation exclusively from PFs,
349 which generated Poisson spike trains, mostly at 10 Hz. In most simulations, this rate
350 was stationary for all but a narrow beam of PFs, the width of which equaled 1/128 of
351 the sagittal circuit length, or about 5.5 μm, comprising < 1% of all PFs. The spike rate
352 within this 'beam' was modulated between 0 and 20 Hz by a sine of period 2048 ms.
353 (Applied periods were powers of 2 (ms) to facilitate application of the Fast Fourier
354 Transform.) This sinusoidal stimulus was used to probe the circuit time-constant in
355 Figs. 4-6.
356
357 *Simulation details.* Simulations were run in GENESIS 2.3 (http://www.genesis-sim.org)
358 using Crank-Nicolson integration in steps of 20 μs (1 μs for voltage clamp). Except
359 when otherwise stated, a circuit of 800 MLIs was simulated with circular boundary
360 conditions along the sagittal axis. Boundary effects along the PF axis, which spanned
361 only five rows of MLIs, were reduced by normalizing the inhibitory connection
362 weights over the actual number of synapses received (this was done separately for the
363 soma and the entire dendritic tree).
364
365 *Data analysis.* The spikes of subpopulations of MLIs, or PFs, were collected over at
366 least 100 periods of the sine stimulus (Fig. 4*B*) and compiled in spike-rate histograms
367 $R(t)$ comprising one period divided into 128 bins (Fig. 4*C*). Since the response
368 frequency was always identical to the stimulus frequency, the response was
369 completely characterized by its amplitude and phase. Polar diagrams (Fig. 4, *D* and *E*)
370 were constructed by plotting the Fourier coefficients (a, b) of the response $R(t)$:

371
$$a = \frac{2}{T}\int_0^T R(t)\cos(\omega t)\,dt$$
$$b = \frac{2}{T}\int_0^T R(t)\sin(\omega t)\,dt$$

372 where ω is the angular frequency (radians s^{-1}, or $\omega/2\pi$ Hz). With this convention the
373 sine-modulated PF activity lies on the positive vertical axis ($a = 0$, $b > 0$) (Fig. 4*D*),
374 and counter-clockwise rotation corresponds to a response *lag*. The mean response of a
375 circuit was the mean vector sum $(\bar{a}, \bar{b})$, in which the anti-phase responses ($a > 0$)
376 were rotated over 180 degrees to prevent them form cancelling the in-phase responses
377 (grey squares in Figs. 4*E* and 6*C*).

378 Because it was not feasible to construct frequency response curves for each
379 parameter setting, the integration time-constants were often estimated from a single
380 frequency of PF stimulation, mostly ~ 0.5 Hz. Under the assumption that the response
381 be generated by a first-order low-pass filter, the integration time-constant τ was
382 assessed as

383
$$\tau = \frac{1}{\omega}\left|\frac{a}{b}\right|.$$

384 Custom-written programs in C were used to analyze the spike trains. The Fast Fourier
385 Transform (Fig. 9) was calculated with the four1 procedure of Press et al. (1992), and
386 the Levenbergh-Marquardt algorithm of Matlab was used for curve-fitting (Figs. 8
387 and 9). All statistics are given as mean ± standard deviation.

388

389 **Results**

390 We conducted large-scale simulations of a circuit of cerebellar molecular-layer
391 interneurons, and assessed the integration time from either the phase lag of its
392 response to a sine-modulated PF beam (Fig. 4-6), the time-course of OFF-beam
393 inhibition evoked by a PF pulse (Fig. 7), or the temporal correlations during spatially
394 uniform random PF excitation (Figs. 8 and 9).

395

396 **Inhibitory coupling of interneurons enhances the circuit time-constant**

397 In a completely disconnected circuit, MLIs responded to a 0.5 Hz sine-modulated PF
398 input with a phase lag of at most 5.7 degrees, corresponding to a time-constant of 32
399 ms. In contrast, the phase lags were considerable in the synaptically connected circuit
400 (Fig. 4).

401 The spike rasterplot (Fig. 4*A*) shows two characteristics of circuits with
402 prolonged integration times. First, the entire circuit is entrained by the sine, even
403 though the stimulus was a narrow PF beam that innervated only 59 of the 800 MLIs.
404 Second, the MLI activity organizes into alternating bands of ON-beam (in-phase) and
405 OFF-beam (anti-phase) activity, the second ON-band around MLI 300 being
406 generated by disinhibition. Figure 4*B* shows the spike-time histograms averaged over
407 a subpopulation of 20 ON-beam MLIs (their position indicated by the black rectangle
408 in *A*) and 20 OFF-beam MLIs (grey rectangle) along with that in the afferent PF
409 beam. Because the inhibition was strong and ON-beam MLIs had only a fraction of
410 their PF inputs modulated by the beam (8 % on average), spiking could persist with
411 less modulation throughout a few cycles (for instance during the first three cycles in
412 Fig. 4, *A* and *B*). Nevertheless, when averaged over 100 cycles, the MLIs clearly

413 modulated their spike rate at the stimulation frequency (Fig. 4*C*), with modulation
414 depths of 46 % and 52 % for ON- and OFF-beam MLIs, respectively.

415 --- Figure 4 about here ---

416 Both ON- and OFF-beam MLIs lagged the PF stimulus, their responses being
417 counter-clockwise rotated on the polar plot (Fig. 4*D*). ON-beam MLIs showed a lesser
418 phase lag than OFF-beam MLIs (45 versus 70 degrees, corresponding to time-
419 constants of 328 versus 915 ms), because they received the zero-phase PF input in
420 addition to the $GABA_A$R-mediated circuit input.

421 Averaged over the entire circuit (Fig. 4*E*) the phase lag measured 59 degrees,
422 corresponding to a time-constant of 542 ms (grey data point). This integration was
423 robust over all temporal frequencies tested: PF stimulation at 0.06 Hz yielded an
424 integration time-constant of 1.07 s.

425

426 **Temporal integration is accomplished through reciprocal inhibition**

427 Weakening the $GABA_A$R synapses (equivalent to applying increasing concentrations
428 of bicuculline) gradually reduced the integration time of both ON- and OFF-beam
429 MLIs (Fig. 5*A*).

430 --- Figure 5 about here ---

431 Because it is difficult to assess the strength of inhibition from experimental data,
432 depending as it is on both synaptic strength and connectivity, we calculated several
433 metrics (such as the variability in spike rate, and the spiking irregularity) that are well
434 known to increase with the level of inhibition (Häusser and Clark 1997) (Fig. 5*B*).
435 When the $GABA_A$R conductance was enhanced, the mean spike rate of the MLIs
436 decreased (Fig. 5*B* left axis) but its standard deviation remained fairly constant so that
437 the relative variation across the circuit increased. At our default strength of 100 %

438 inhibition, the MLIs fired 13.0 ± 11.2 spikes s^{-1}. Stronger inhibition also made the
439 MLIs spike more irregularly, as measured from the variation in duration of
440 consecutive inter-spike intervals (CV2) (Fig. 5*B*, right axis). As opposed to the
441 regular spiking of MLIs when all inhibition was blocked (CV2 of 0.34 ± 0.01), MLIs
442 in the standard circuit spiked with a CV2 of 0.87 ± 0.13.

443 By changing the level of PF excitation, slow integration could be generated with
444 MLIs spiking at rates ranging from 10 to > 60 s^{-1} (Fig. 5*C*). Forty Hz PF input, for
445 instance, generated a circuit time-constant of 0.98 s with MLIs spiking on average at
446 42 s^{-1}.

447

448

449 **The circuit time-constant critically depends on the position of axonal boutons**

450 A critical parameter was the connection kernel, and more particularly the average
451 connection distance, which determined the balance between self and lateral inhibition.
452 Because the proximal axonal plexus was centered only 40 μm from the soma, it would
453 lay many synapses on MLIs with an overlapping dendrite (left MLI in Fig. 6*A*).
454 According to Cannon et al. (1983), shared inputs between inhibitory neurons are
455 transmitted with a fast time-constant (Fig. 1). In agreement with this, slow integration
456 was only observed when the connections were laid predominantly by the distal axonal
457 plexus centered 160 μm from the soma (see bouton positions of right MLI in Fig. 6*A*).

458 --- Figure 6 about here ---

459 Accordingly, the integration time decreased from 541 to 65 ms when the
460 average connection distance was reduced form 131.8 to 80 μm, the latter value being
461 less than the 86 μm sagittal width of the dendrite. For reference, the diamond and

462 horizontal bar in Fig. 6*A* denote the mean and variation across MLIs in the sample of
463 Sultan and Bower (1998).

464 Although autapses are a form of self-inhibition, their very number was not a
465 critical parameter (Fig. 6*B*). By narrowing the transverse width of the connection
466 kernel, the number of autapses could be increased without enhancing the overall
467 amount of self-inhibition, and hence without affecting the integration time.

468 Evidently, increasing the sagittal length of the circuit would make it more
469 difficult for a narrow PF beam to entrain the entire circuit. Nevertheless temporal
470 integration could be completely restored by stimulating several PF beams at regular
471 intervals simultaneously (Fig. 6*C*). This circuit of 1600 MLIs was stimulated by three
472 PF beams about 400 μm apart and had an average integration time of 1.556 s (grey
473 data point).

474

475 **Responses of MLIs to pulse stimulation of the parallel-fiber beam**

476 We simulated pulse-like PF stimulation in an MLI circuit with a lower (50 %)
477 baseline level of PF activity to minimize the position effects which lateral inhibition
478 may induce even in a uniformly excited circuit (see for instance Fig. 4*A*, where lateral
479 inhibition induced a spatial patterning in addition to the stimulus-modulated temporal
480 patterning).

481 --- Figure 7 about here ---

482 Figure 7 plots the MLI responses to a 50 ms PF pulse, measured at three
483 distances for three levels of inhibition. An excitatory response was seen in MLIs
484 located up to 69 μm from the center of the stimulated PF beam (*a*). Farther away up to
485 277 μm, the response was a sharp depression followed by a slow recovery to baseline
486 (*b*). This OFF zone was flanked by a ~ 100 μm wide ON zone of disinhibition, where

487 response amplitudes reached at most 22 % of those ON-beam (*c*). With full-blown
488 inhibition (100 %), the OFF-beam rise-time (time to 1/*e* recovery) measured ~ 340
489 ms, but also the ON-beam response had a slow component of ~ 240 ms.
490
491
492
493 **Using the spike-train autocorrelogram to estimate the circuit time-constant**
494 An alternative method to estimate integration time is to dismiss the PF beam and
495 apply stationary Poisson input throughout. Integration is then manifest as a slowly
496 decaying central peak on the autocorrelogram. Figure 8*A* plots the results of this
497 analysis for the same circuit that had been tested with a sine-modulated PF beam in
498 Figs. 4 and 5.
499 --- Figure 8 about here ---
500 The 800 MLIs were divided into subpopulations of 20 MLIs with like sagittal
501 position, and for each sub-population the time-constant and depth of spike-rate
502 modulation were derived from the exponential function fitted to the autocorrelogram
503 (see examples a-d in *inset* to Fig. 8*A*). The average time-constant measured 1262 ±
504 493 ms with full-blown inhibition, but fell to 60.2 ± 20.3 ms when the $GABA_AR$
505 conductance was reduced to 20 %.
506
507 **Electrical coupling enhances the integration time**
508 When all gap junctions were blocked, the average time-constant dropped to 899.7 ±
509 320.4 ms, and the modulation depth (a metric for the fraction of spikes involved in
510 integration) from 95 % to 45 % (compare upper and lower panels of Fig. 8*A*). With
511 half of the gap junctions blocked randomly (resulting in MLIs having 5.75 ± 1.78

512 electrical synapses), integration time and modulation depth still measured 1173 ms
513 and 68 %.

514 In contrast, deleting the gap junctions had no effect on synchronization. Figure
515 8*B* shows high central peaks (width < 2 ms) on the cross-correlograms between
516 nearby groups of MLIs, in both coupled (left, central peak height 340 % above
517 baseline) and uncoupled circuits (right, height 344 %). Electrically coupled circuits
518 further always had a slightly reduced average spike rate (13.0 *versus* 14.6 s^{-1} in Fig.
519 8*A*), because, as shown in greater detail in Fig. 8*C,* gap junctions were more effective
520 in spreading (mostly slow) hyperpolarizing than (fast) depolarizing currents.

521 Even in a purely electrically coupled circuit (black traces in Fig. 8*C*), an action
522 potential, here evoked in MLI 233, induced a more substantial hyper- than de-
523 polarization in both a mono-synaptic target (MLI 238, negative surface area of black
524 trace greater than positive area by a factor of 3) and a di-synaptic target (MLI 258,
525 relative factor 4.3). In the $GABA_A$R-connected circuit, this predominance of
526 inhibition over excitation was even greater (grey traces, factors of 7.7 and 92.4,
527 respectively). Note that neither MLI 238 nor MLI 258 received $GABA_A$R synapses
528 from MLI 233, so their IPSP-like potentials were transmitted electrically (di-
529 synaptically to MLI 258, tri-synaptically to MLI 238). This electric transmission
530 induced a slow capacitive current that substantially prolonged the time-course of these
531 secondary IPSPs (peak at 22 ms and decay time of 32 ms for MLI 258).

532

533 **MLI spike trains show approximately 1/*f* power scaling at low frequencies**

534 The power spectrograms, calculated from the spike-time histograms, displayed a
535 (close to) 1/*f* scaling at low frequencies. Figure 9*A* plots for each of the 40
536 subpopulations of MLIs the exponent *n* of the function f^{n} that best fitted the

spectrogram within the frequency range of 0.5-15 Hz. Examples of spectrograms (a, b, c, d) and of the fitted functions, are shown on log-log plots in Fig. 9, *B* and *C*. When inhibition was reduced to 20 %, the mean slope dropped from -0.88 ± 0.09 to -0.47 ± 0.04 (Fig. 9*D*).

--- Figure 9 about here ---

With all inhibition blocked the power spectrum was flat over the entire low-frequency domain (slope of + 0.02) (Fig. 9, *D*-*F*). The 1/*f* power scaling did not require the neurons to have dendrites, as mean slopes of -0.95 were still measured in circuits of MLIs whose axial dendritic resistances had been reduced from 240 MΩ to 1 Ω to abolish all passive dendritic filtering (the dendrites were given their normal morphology to preserve the synaptic connections).

Robustness of temporal integration

Several neuron, synapse and circuit parameters were varied, and their qualitative effects on the integration time are summarized in Table 2. The critical dependence on the strength of inhibition and the shape of the connection kernel (entries 1 and 6, see also Figs. 5 and 6) is at the core of the model by Cannon et al. (1983). Cannon and Robinson (1985) also recognized the need for uniformity, as neurons of a too heterogeneous circuit would integrate their noise (entries 3 and 7).

--- Table 2 about here ---

New is our finding that too strong inhibition impairs integration in a biophysically realistic circuit (Fig. 5*A*) because the weaker neurons are silenced so fast that the circuit functionally disconnects before the integration is completed (Fig. 1).

562 **Effects on a readout Purkinje cell**

563 At varying positions along the sagittal axis, a reduced 339-compartmental model PC
564 (see Maex and Steuber 2013) was inserted into the MLI circuit. Feed-forward
565 connections were made from the MLI axonal kernels, but without laying feedback
566 connections from PCs to MLIs (Lemkey-Johnston and Larramendi 1968; Witter et al.
567 2016) or to the sources of PFs, granule cells (Guo et al. 2016).

568 The PCs showed a variety of responses to pulse (Fig. 10*A*) and sinusoidal PF
569 stimulation (Fig. 10, *B* and *D*), depending on their balance between PF excitation and
570 MLI inhibition.

571 --- Figure 10 about here ---

572 With inhibition predominant (Fig. 10, *A* and *B*), the PC responses mimicked those of
573 MLIs. PC1, which received only weak ON-beam PF excitation (2.7 % of its afferent
574 PFs being part of the beam), produced a multiphasic response to the PF pulse (Fig.
575 10*A*) and a 6 % modulated, in-phase sine response that lagged the PF input by 39
576 degrees (Fig. 10*B*). As for PC2 and PC3, neither received monosynaptic input from
577 the PF beam. PC2, receiving most of its inhibition from anti-phase MLIs, exhibited a
578 disinhibitory pulse response and a 14 % modulated, in-phase sine response lagging
579 the PF input by 51 degrees. In contrast, PC3, which received inhibition primarily from
580 in-phase MLIs, recovered only slowly from a deep depression during the pulse (Fig.
581 10*A*); its 21 % modulated, anti-phase sine response had a phase lag of 54 degrees (or,
582 equivalently, a 126-degree phase lead). Hence both in-phase (PC2) and anti-phase
583 lagging PC responses (PC3) could be generated, reminiscent of the responses of mice
584 PCs that lag either ipsiversive or contraversive head velocity during the vestibulo-
585 ocular reflex (Katoh et al. 2015).

586 With stronger PF excitation (Fig. 10*D*), PCs could be made to phase-lead their
587 PF input, as can easily be understood from the vector summation of PF inputs and
588 anti-phase MLI responses on the polar diagram in Fig. 10*C*. PCs 4 and 5 led their PF
589 input by 18 and 26 degrees, respectively, for modulation depths of 9 and 16 %. Both
590 PCs received 10.1 % of their PF inputs from the beam, but the strength of inhibition
591 had been reduced by 50 % for PC4 and by 25 % for PC 5.

592 **Discussion**

593 MLIs are classically regarded to mediate fast di-synaptic inhibition from parallel
594 fibers to Purkinje cells (Carter and Regehr 2002; Isope et al. 2002; Mittmann et al.
595 2005; Blot et al. 2016), and, through their precise timing, to control the kinematics of
596 movements (Heiney et al. 2014). The present modeling study predicts that the MLI
597 circuit may also generate slow response components with time-constants up to 1.5
598 seconds. In addition to enhancing the circuit time-constant, lateral inhibition in the
599 present model induced ON and OFF responses and enhanced the phase-diversity of
600 the PC response. As such the interneuron circuit of the molecular layer could function
601 as an adaptive filter (Fujita 1982; Dean et al. 2010), a function that has also been
602 attributed to the granular layer (Bratby et al. 2016), more particularly to its Golgi cells
603 (Miles et al. 1980; Fujita 1982; Heine et al. 2010) and unipolar brush cells (Zampini
604 et al. 2016).

605

606 **Model constraints for temporal integration**

607 In many respects, the present circuit model is a biophysical implementation of the
608 analytical model by Cannon, Robinson and Shamma (1983), of which it inherits the
609 two principal parameters: the average connection distance, which sets the balance
610 between self and lateral inhibition, and the strength of inhibition, which tunes the
611 circuit time-constant.

612 Figure 6*A* showed that temporal integration required the average connection
613 distance of the $GABA_AR$ synapses to be greater than the sagittal width of the dendritic
614 tree (86 μm in the present model). In adult rats, Sultan and Bower (1998) found that
615 axonal boutons were located on average 91 ± 67 μm from the soma, for "a continuous
616 transition of axonal distribution functions from those with more local (close to the

617 dendrite) to more nonlocal distributions". In addition there was a greater variation in
618 axonal than dendritic spread (see their Fig. 7*D* where axons could extend from < 100
619 to > 500 μm). In juvenile (postnatal day P11-P14) rats, most of the (on average 68)
620 boutons were located in the second and third quadrants along axons of on 211.7 ±
621 54.9 μm sagittal spread, which again would give a mean bouton distance of around
622 100 μm (Zorrilla de San Martin et al. 2015). Based on these data, therefore, only a
623 fraction of the MLIs, those with the longest axons, should be involved in temporal
624 integration. On the other hand, most electrophysiological and optical measurements of
625 the spread of inhibition reported values greater than the 277 μm in the present model
626 (see Fig. 7): from about 300 μm (Kim et al. 2014), to > 480 μm (Dizon and
627 Khodakhah 2011), 500 μm (in cats) (Andersen et al. 1964) and 800 μm (in guinea
628 pigs) (Cohen and Yarom 2000). Note that the connection kernel in Cannon et al.
629 (1983) also had a central notch (their Fig. 2*C*), the width of which related inversely to
630 the optimal spatial frequency for the stimulus. Their stimulus being a spatial grating
631 that excited point neurons, this notch should be convolved with the dendritic width,
632 which hence sets a lower bound on the mean distance of the lateral connections.

633 The second critical parameter, the strength of inhibition, depends on the number
634 and strength of the $GABA_AR$ synapses, the values of which have been thoroughly
635 motivated in the Methods section. An indirect assessment of the strength of inhibition
636 is provided by the rate and regularity of firing (Häusser and Clark 1997). Our default
637 model, stimulated with 10 Hz PF input, produced a mean MLI spike rate of 13.0 ±
638 11.2 s^{-1} (Fig. 5*B*). These values are close to those measured in anaesthetized mice and
639 rats (10 ± 10.9 and 4.8 ± 6.6 s^{-1} for stellate and basket cells in Barmack and Yakhnitsa
640 (2008); 13.7 ± 12.5 and 9.9 ± 10.1 s^{-1} for stellate and basket cells in Ruigrok et al.
641 (2011); 9.8 ± 3.6 and 5.5 ± 1.9 s^{-1} for MLIs in lobules VI/VII and X, respectively, in

642 Witter and De Zeeuw (2015)). By further enhancing the PF spike rate in the model,
643 much higher MLI spike rates could be obtained (> 60 s^{-1}), comparable to those
644 observed in awake and behaving animals (Ozden et al. 2012; Badura et al. 2013; ten
645 Brinke et al. 2015; Jelitai et al. 2016), without any decline in integration time (Fig.
646 5*C*).

647 Likewise, the CV_2 metric of spiking irregularity measured 0.87 ± 0.13 in the
648 standard circuit (Fig. 5*B*), which is comparable to the in-vivo measured values (0.93 ±
649 0.15 and 0.64 ± 0.19 in Witter and De Zeeuw (2015), 0.76 ± 0.21 and 0.65 ± 0.23 in
650 Ruigrok et al. (2011), and 0.66 in ten Brinke et al. (2015)).

651

652 **Developmental changes**

653 Most in vitro data on MLIs have been obtained in young animals, and although the
654 MLI-PC synapse has been shown to decrease in strength with maturation (Pouzat and
655 Hestrin 1997), this is not the case for the $GABA_AR$ synapses among MLIs: Astori et
656 al. (2009) found an *increase* in both the frequency of miniature IPSCs and in the
657 amplitude of evoked IPSCs between postnatal days 14 and 28.

658 In the analytical model of Cannon et al. (1983), neurons inhibit each other in a
659 continual and graded fashion, not pulse-like as do actual neurons. A failure to provide
660 continual inhibition may have underlain the breakdown of integration at very low
661 MLI spike rates (Fig. 5*C*). It is tempting to consider that a similar situation may occur
662 during early development when the connectivity among MLIs and the mIPSC
663 frequency are sparse (Astori et al. 2009), and to interpret several characteristics of the
664 immature circuit as compensations for this sparseness (thereby tacitly assuming that
665 activation of $GABA_ARs$ is already inhibitory at this stage). In young animals,
666 $GABA_AR$ synapses have a slower kinetics (the current decaying five time slower at

667 P11 than at P35 in Vicini et al. (2001)), a higher release probability (Liu and Lachamp
668 2006), and a lower failure rate (Pouzat and Hestrin 1997). Before postnatal day P15,
669 presynaptic $GABA_A$ autoreceptors (Pouzat and Marty 1999) enhance GABA release,
670 increase MLI excitability (Zorrilla de San Martin et al. 2015) and induce doublet
671 firing (Mejia-Gervacio and Marty 2006), under the assumption that axonal GABA is
672 still excitatory because of an enhanced axonal Cl^- concentration, as argued in Zorrilla
673 de San Martin et al. (2015). Finally, presynaptic NMDA receptors in juvenile animals
674 may enhance GABA release and regulate plasticity (Fiszman et al. 2005; Liu 2007;
675 Rossi et al. 2012).

676 Likewise, younger animals are more tightly coupled by gap junctions (van der
677 Giessen et al. 2006). In contrast, the number of MLIs making autapses increases with
678 age (Pouzat and Marty 1998), and although self-inhibition tends to decrease the
679 circuit time-constant, this number was not a very restrictive parameter (Fig. 6*B*).

680

681 **Limitations of the present study**

682 The present modeling study shows that temporal integration is a feasible function of
683 interneuron circuits under the constraints mentioned above. Some physiological
684 components were, for economy, not included in the model, but their effects can be
685 predicted from the above analysis.

686 Slow excitatory currents, or currents with a self-excitatory component, are
687 expected to enhance the circuit time-constant. Examples are: persistent Na currents
688 (Mann-Metzer and Yarom 2002a), currents underlying spike-rate acceleration (Mann-
689 Metzer and Yarom 2000; Jörntell and Ekerot 2003), currents through metabotropic
690 glutamate receptors (Collin et al. 2009) or dendritic NMDA receptors (Clark and
691 Cull-Candy 2002; Szapiro and Barbour 2007), and $GABA_AR$-mediated potentiation of

692 glutamate release by PFs (Stell 2011; Astorga et al. 2015). In contrast, currents with a
693 self-inhibitory component will reduce the time-constant, such as currents underlying
694 (decelerating) spike-rate adaptation (Witter and De Zeeuw 2015) or currents through
695 $GABA_B$ autoreceptors (Mann-Metzer and Yarom 2002b; Astori et al. 2009).

696 The present study indicates that homeostatic mechanisms that control the gain
697 of the circuit may also regulate its integration time. Such homeostatic mechanisms
698 include the spillover of GABA to PF varicosities, which has been observed to
699 suppress long-term glutamate release (Berglund et al. 2016; Howell and Pugh 2016),
700 and the spillover of glutamate to MLI axon terminals, which induces either an
701 AMPAR-mediated inhibition of evoked GABA release in young animals (Liu 2007;
702 Rigby et al. 2015) or an NMDAR-mediated LTP in adults animals (Dubois et al.
703 2016). Calcium influx into the dendrites, either through AMPA (Soler-Llavina and
704 Sabatini 2006) or NMDA receptors (Tran-Van-Minh et al. 2016), has been observed
705 to depress PF synapses.

706 A poorly known factor is the natural spatial pattern of PF activity. With the
707 uniform baseline PF excitation used in the present study, spatial patterns of MLI
708 activity would spontaneously arise at levels of inhibition needed for temporal
709 integration (Fig. 4*A*). Since these patterns depended on the boundary conditions
710 (including circuit length), stimulus position was in fact indeterminate. We should
711 therefore assume either that such patterns (alternating along the sagittal axis, oriented
712 along the folial axis) are hard-wired, for instance by gradients in the expression of ion
713 channels, or, more likely, that the PF stimulus is patterned itself. A grating pattern of
714 PF activity, as used for the simulation of the 1600-MLI circuit in Fig. 6*C*, could be
715 generated by the many rosettes that each mossy fiber gives off along its sagittal course
716 through the folium (Sultan 2001). This way, the signals of granule cells at different

717 sagittal positions could also be filtered with slightly different time-constants (Fig.
718 6*C*), enabling PCs to learn to recognize temporal patterns through plasticity of the PF-
719 MLI or MLI-PC synapse (Jörntell et al. 2010).
720

721 **Electrophysiological and behavioral relevance**

722 Imaging the response of the molecular layer to brief PF pulses has been used to infer
723 the function of MLIs (Cohen and Yarom 2000; Sullivan et al. 2005; Gao et al. 2006).
724 As in the present model (Fig. 7), OFF-beam inhibition can last tens to hundreds of
725 milliseconds and spread over distances of several hundreds of micrometers in the
726 sagittal direction. The recovery time of 340 ms in the present model (Fig. 7) was
727 slower than the 100-140 ms measured in the first imaging experiments by Cohen and
728 Yarom (2000), but this value could is sensitive to the level of inhibition (Fig. 7*C*). Of
729 particular relevance is the imaging study by Sullivan et al. (2005), which found
730 prolonged Ca^{2+} responses in ON-beam MLIs over a half-width equal to that in the
731 present study (~ 70 μm). The authors attributed the slow time-course, however, to the
732 activation of NMDARs by spilled-over glutamate.

733 Barmack and Yakhnitsa (2008; 2013) recorded stellate and basket cells in
734 mouse uvula-nodulus during 0.2 Hz vestibular rotation, and found that their responses
735 lagged, by 32 and 42 degrees, those of the climbing fibers by which they were
736 primarily driven. This phase lag corresponds to a low-pass time-constant of ~ 0.5 s,
737 which, according to the present model (and substituting climbing fibers for PFs as the
738 major source of excitation) may be generated by the MLI circuit. The preferred
739 orientations in those vestibular experiments were distributed over three quadrants
740 (Fig. 9*D* in Barmack and Yakhnitsa (2008)), but such a broad distribution of phases
741 can be reproduced by the model as well (Figs. 4*E* and 6*C*).

742 A role of MLIs in setting the phase of the PC response has been suggested
743 before. In humans wearing vision-reversing glasses, Melvill Jones and colleagues
744 observed a phase-lag of the vestibulo-ocular reflex (VOR) that developed over the
745 course of days to weeks (Davies and Jones 1976; Gonshor and Jones 1976). They
746 proposed a simple linear model, which explained the changes in both gain and phase
747 by a gradual adaptation of the relative weights of the two major inputs to the
748 vestibular nuclei: the primary vestibular signal, the weight of which would decrease in
749 strength, and the negative copy from PCs. Importantly, the model required a fixed
750 (non-adaptive) phase lead of the PC signal, which could be achieved through
751 inhibition of the PCs by a process with a time-constant of about one second. The
752 authors suggested that this phase lead was generated through "basket and superficial
753 stellate cell inhibition of Purkinje cells" (Gonshor and Jones 1976, pp 406-7).

754 Wulff et al. (2009) found that phase-reversal learning of the VOR was abolished
755 in transgenic mice whose PCs lacked $GABA_A$Rs. Nevertheless, the phase of the PC
756 response was largely preserved, indicating that the circuit is more complex and can
757 partially recover by input from (non-modeled) climbing fibers (Badura et al. 2013;
758 Barmack and Yakhnitsa 2013). Their mouse strain, and another strain with reduced
759 MLI inhibition to PCs (Badura et al. 2016), also showed impaired eye-blink
760 conditioning (ten Brinke et al. 2015). Whether the MLIs contribute to the timing of
761 conditional responses is still a matter of debate (Johansson et al. 2015), but according
762 to the present model, the MLI circuit could generate the required response delays. In
763 Fig. 10*A*, for instance, PC3 recovered only slowly from its depression during the
764 pulse, a feature that is also seen on simple-spike traces following the conditional
765 stimulus (ten Brinke et al. 2015).

766

767 **The function of electrical coupling in inhibitory circuits**

768 The present study offers an alternative explanation for the abundance of gap junctions
769 in interneuron circuits in cerebellar (Mann-Metzer and Yarom 1999; Rieubland et al.
770 2014) and cerebral cortex (Galarreta and Hestrin 1999; Gibson et al. 1999). Two
771 mechanisms may underlie the additional increase in integration time observed when
772 the inhibitory circuit was also coupled electrically (Fig. 8*A*). First, electrically
773 transmitted IPSPs had a particularly slow time-course (Fig. 8*C*), as the electrical
774 coupling enhanced the effective membrane capacitance (Alcami and Marty 2013).
775 Since in the analytical model by Cannon et al. (1983) reciprocal inhibition enhances
776 the time-constant in a multiplicative manner, any slow process in the basic circuit may
777 have a considerable effect on the final integration time. Second, we often observed
778 that electric coupling limited the heterogeneity of the circuit, especially when
779 inhibition was strong. Cannon and Robinson (1985) recognized that too great
780 heterogeneity could be a problem, as neurons would start integrating the 'noise' rather
781 than the stimuli. Whether electric coupling itself can be a source of heterogeneity
782 among interneurons, as suggested by Vervaeke et al. (2010), may depend on their
783 strength, variability and number.

784 The sharp synchronization between neighboring MLIs (Fig. 8*B*), comparable to
785 that observed in tetrode-recordings in anaesthetized rats (Blot et al. 2016), can be
786 explained by shared synaptic excitation and inhibition (Maex et al. 2000), without
787 having to invoke fast electrical transmission of action potentials. This may seem at
788 odds with the conclusions of a study on synchronization between Golgi cells (van
789 Welie et al. 2016), but the model used in that study privileged electrical
790 synchronization through the use of stronger gap junctions (330 pS vs. 200 pS in the
791 present study), broader dendrites (1 vs. 0.4 μm diameter), and weaker chemical

792 synapses (peak conductances of 0.25 vs. 1.8 nS for AMPARs, and 0.25 vs. 2.77 ns for
793 $GABA_A$Rs).
794
795
796 **A model prediction: 1/f power scaling**
797 A very robust but unexpected finding was the inverse scaling of power with frequency
798 on the spike-train spectrogram (Fig. 9). We briefly consider four not mutually
799 exclusive interpretations of this low-frequency predominance. A first explanation
800 would be that inhibition, by its single effect of lowering the spike rate, concomitantly
801 moves the power to lower frequencies, as in Fig. 9*D*. There was, however, no
802 relationship between the power exponent and the spike rate within the circuit analyzed
803 in Fig. 9A: the subpopulation of MLIs having the highest rate also had one of the
804 steepest slopes. Secondly, one might interpret the *1/f* scaling as caused by slow circuit
805 oscillations. Although slow oscillations were often observed in free-running circuits,
806 they were fleeting and of varying frequency. A third interpretation uses the context of
807 catastrophe theory (Baranauskas et al. 2012). Here it is thought that strong inhibition
808 promotes the switching of neurons between ON and OFF states. Such switching could
809 occasionally be observed (Fig. 4*A*), and it may account for some of the shallow slopes
810 on the autocorrelograms (Fig. 8*A* inset), as indeed a rectangular time-pattern has a
811 triangular autocorrelogram. Interestingly, concomitant signs of scale invariance
812 (Kekovic et al. 2010) and slow-frequency dominance (Culic et al. 2005; Abrams et al.
813 2012) have been observed in cerebellar recordings. Finally, the most conservative
814 conclusion is that the *1/f* spectrogram is a mere reflection of the rise in integration
815 time caused by reciprocal inhibition. Since lateral inhibition is a widespread
816 phenomenon, it could also underlie the *1/f* scaling that has been reported in many

817 surface recordings (see for instance Novikov et al. 1997). According to the present
818 model this scaling may be generated by temporal integration in interneuron circuits.
819

820 **Acknowledgements**

821 We thank P. Gonçalves for comments on an earlier draft of this manuscript.
822

823 **Grants**

824 This work was conducted as part of project ANR-13-BSV4-0016 CerebComp, and
825 partly supported by ANR-10-LABX-0087 IEC and ANR-10-IDEX-0001-02 PSL (all
826 France).
827

828 **Disclosures**

829 The authors declare no competing financial interests.
830
831

832 **References**

833

834 **Abrahamsson T, Cathala L, Matsui K, Shigemoto R, and DiGregorio DA**. Thin
835 dendrites of cerebellar interneurons confer sublinear synaptic integration and a
836 gradient of short-term plasticity. *Neuron* 73: 1159-1172, 2012.

837 **Abrams ZR, Warrier A, Wang Y, Trauner D, and Zhang X**. Tunable oscillations
838 in the Purkinje neuron. *Phys Rev E Stat Nonlin Soft Matter Phys* 85: 041905, 2012.

839 **Alcami P, and Marty A**. Estimating functional connectivity in an electrically
840 coupled interneuron network. *Proc Natl Acad Sci U S A* 110: 4798-4807, 2013.

841 **Andersen P, Eccles JC, and Voorhoeve PE**. Postsynaptic inhibition of cerebellar
842 Purkinje cells. *J Neurophysiol* 27: 1138-1153, 1964.

843 **Anderson D, Mehaffey WH, Iftinca M, Rehak R, Engbers JD, Hameed S,**
844 **Zamponi GW, and Turner RW**. Regulation of neuronal activity by Cav3-Kv4
845 channel signaling complexes. *Nat Neurosci* 13: 333-337, 2010.

846 **Astorga G, Bao J, Marty A, Augustine GJ, Franconville R, Jalil A, Bradley J,**
847 **and Llano I**. An excitatory GABA loop operating *in vivo*. *Front Cell Neurosci* 9:
848 275, 2015.

849 **Astori S, Lujan R, and Kohr G**. GABA release from cerebellar stellate cells is
850 developmentally regulated by presynaptic GABA(B) receptors in a target-cell-specific
851 manner. *Eur J Neurosci* 30: 551-559, 2009.

852 **Badura A, Clopath C, Schonewille M, and De Zeeuw CI**. Modeled changes of
853 cerebellar activity in mutant mice are predictive of their learning impairments. *Sci*
854 *Rep* 6: 36131, 2016.

855 **Badura A, Schonewille M, Voges K, Galliano E, Renier N, Gao Z, Witter L,**
856 **Hoebeek FE, Chedotal A, and De Zeeuw CI**. Climbing fiber input shapes
857 reciprocity of Purkinje cell firing. *Neuron* 78: 700-713, 2013.
858 **Baranauskas G, Maggiolini E, Vato A, Angotzi G, Bonfanti A, Zambra G,**
859 **Spinelli A, and Fadiga L**. Origins of $1/f^2$ scaling in the power spectrum of
860 intracortical local field potential. *J Neurophysiol* 107: 984-994, 2012.
861 **Bardoni R, and Belluzzi O**. Kinetic study and numerical reconstruction of A-type
862 current in granule cells of rat cerebellar slices. *J Neurophysiol* 69: 2222-2231, 1993.
863 **Barmack NH, and Yakhnitsa V**. Functions of interneurons in mouse cerebellum. *J*
864 *Neurosci* 28: 1140-1152, 2008.
865 **Barmack NH, and Yakhnitsa V**. Modulated discharge of Purkinje and stellate cells
866 persists after unilateral loss of vestibular primary afferent mossy fibers in mice. *J*
867 *Neurophysiol* 110: 2257-2274, 2013.
868 **Berglund K, Wen L, Dunbar RL, Feng G, and Augustine GJ**. Optogenetic
869 visualization of presynaptic tonic inhibition of cerebellar parallel fibers. *J Neurosci*
870 36: 5709-5723, 2016.
871 **Bishop GA**. An analysis of HRP-filled basket cell axons in the cat's cerebellum. I.
872 Morphometry and configuration. *Anat Embryol (Berl)* 188: 287-297, 1993.
873 **Blot A, de Solages C, Ostojic S, Szapiro G, Hakim V, and Lena C**. Time-invariant
874 feed-forward inhibition of Purkinje cells in the cerebellar cortex in vivo. *J Physiol*
875 594: 2729-2749, 2016.
876 **Bratby P, Sneyd J, and Montgomery J**. Computational architecture of the granular
877 layer of cerebellum-like structures. *Cerebellum* 2016.

878 **Briatore F, Patrizi A, Viltono L, Sassoe-Pognetto M, and Wulff P**. Quantitative
879 organization of GABAergic synapses in the molecular layer of the mouse cerebellar
880 cortex. *PLoS One* 5: e12119, 2010.
881 **Cannon SC, and Robinson DA**. An improved neural-network model for the neural
882 integrator of the oculomotor system: more realistic neuron behavior. *Biol Cybern* 53:
883 93-108, 1985.
884 **Cannon SC, Robinson DA, and Shamma S**. A proposed neural network for the
885 integrator of the oculomotor system. *Biol Cybern* 49: 127-136, 1983.
886 **Carter AG, and Regehr WG**. Quantal events shape cerebellar interneuron firing. *Nat*
887 *Neurosci* 5: 1309-1318, 2002.
888 **Carzoli KL, and Liu J**. Alterations in cerebellar stellate cell hyperpolarization-
889 activated currents following fear learning. In: *Society for Neuroscience Abstracts*.
890 Chicago: Society for Neuroscience, 2015, p. 35.28.
891 **Chan-Palay V, and Palay SL**. The stellate cells of the rat's cerebellar cortex. *Z Anat*
892 *Entwicklungsgesch* 136: 224-248, 1972.
893 **Clark BA, and Cull-Candy SG**. Activity-dependent recruitment of extrasynaptic
894 NMDA receptor activation at an AMPA receptor-only synapse. *J Neurosci* 22: 4428-
895 4436, 2002.
896 **Cohen D, and Yarom Y**. Cerebellar on-beam and lateral inhibition: two functionally
897 distinct circuits. *J Neurophysiol* 83: 1932-1940, 2000.
898 **Collin T, Franconville R, Ehrlich BE, and Llano I**. Activation of metabotropic
899 glutamate receptors induces periodic burst firing and concomitant cytosolic Ca^{2+}
900 oscillations in cerebellar interneurons. *J Neurosci* 29: 9281-9291, 2009.

901 **Culic M, Blanusa LM, Grbic G, Spasic S, Jankovic B, and Kalauzi A**. Spectral
902 analysis of cerebellar activity after acute brain injury in anesthetized rats. *Acta*
903 *Neurobiol Exp (Wars)* 65: 11-17, 2005.

904 **Davies P, and Jones GM**. An adaptive neural model compatible with plastic changes
905 induced in the human vestibulo-ocular reflex by prolonged optical reversal of vision.
906 *Brain Res* 103: 546-550, 1976.

907 **De Zeeuw CI, Wylie DR, Stahl JS, and Simpson JI**. Phase relations of Purkinje
908 cells in the rabbit flocculus during compensatory eye movements. *J Neurophysiol* 74:
909 2051-2064, 1995.

910 **Dean P, Porrill J, Ekerot CF, and Jörntell H**. The cerebellar microcircuit as an
911 adaptive filter: experimental and computational evidence. *Nat Rev Neurosci* 11: 30-
912 43, 2010.

913 **Dieudonné S**. Submillisecond kinetics and low efficacy of parallel fibre-Golgi cell
914 synaptic currents in the rat cerebellum. *J Physiol* 510: 845-866, 1998.

915 **Dizon MJ, and Khodakhah K**. The role of interneurons in shaping Purkinje cell
916 responses in the cerebellar cortex. *J Neurosci* 31: 10463-10473, 2011.

917 **Dubois CJ, Lachamp PM, Sun L, Mishina M, and Liu SJ**. Presynaptic GluN2D
918 receptors detect glutamate spillover and regulate cerebellar GABA release. *J*
919 *Neurophysiol* 115: 271-285, 2016.

920 **Eccles JC, Llinás R, and Sasaki K**. The inhibitory interneurones within the
921 cerebellar cortex. *Exp Brain Res* 1: 1-16, 1966.

922 **Fiszman ML, Barberis A, Lu C, Fu Z, Erdélyi F, Szabó G, and Vicini S**. NMDA
923 receptors increase the size of GABAergic terminals and enhance GABA release. *J*
924 *Neurosci* 25: 2024-2031, 2005.

925 **Fujita M**. Adaptive filter model of the cerebellum. *Biol Cybern* 45: 195-206, 1982.

926 **Gabbiani F, Midtgaard J, and Knöpfel T**. Synaptic integration in a model of
927 cerebellar granule cells. *J Neurophysiol* 72: 999-1009, 1994.
928 **Galarreta M, and Hestrin S**. A network of fast-spiking cells in the neocortex
929 connected by electrical synapses. *Nature* 402: 72-75, 1999.
930 **Gao W, Chen G, Reinert KC, and Ebner TJ**. Cerebellar cortical molecular layer
931 inhibition is organized in parasagittal zones. *J Neurosci* 26: 8377-8387, 2006.
932 **Gibson JR, Beierlein M, and Connors BW**. Two networks of electrically coupled
933 inhibitory neurons in neocortex. *Nature* 402: 75-79, 1999.
934 **Giovannucci A, Badura A, Deverett B, Najafi F, Pereira TD, Gao Z, Ozden I,**
935 **Kloth AD, Pnevmatikakis E, Paninski L, De Zeeuw CI, Medina JF, and Wang**
936 **SS**. Cerebellar granule cells acquire a widespread predictive feedback signal during
937 motor learning. *Nat Neurosci* 2017.
938 **Gonshor A, and Jones GM**. Extreme vestibulo-ocular adaptation induced by
939 prolonged optical reversal of vision. *J Physiol* 256: 381-414, 1976.
940 **Guo C, Witter L, Rudolph S, Elliott HL, Ennis KA, and Regehr WG**. Purkinje
941 cells directly inhibit granule cells in specialized regions of the cerebellar cortex.
942 *Neuron* 2016.
943 **Häusser M, and Clark BA**. Tonic synaptic inhibition modulates neuronal output
944 pattern and spatiotemporal synaptic integration. *Neuron* 19: 665-678, 1997.
945 **Heine SA, Highstein SM, and Blazquez PM**. Golgi cells operate as state-specific
946 temporal filters at the input stage of the cerebellar cortex. *J Neurosci* 30: 17004-
947 17014, 2010.
948 **Heiney SA, Kim J, Augustine GJ, and Medina JF**. Precise control of movement
949 kinematics by optogenetic inhibition of Purkinje cell activity. *J Neurosci* 34: 2321-
950 2330, 2014.

951 **Hirano T, and Hagiwara S**. Kinetics and distribution of voltage-gated Ca, Na and K
952 channels on the somata of rat cerebellar Purkinje cells. *Pflugers Arch* 413: 463-469,
953 1989.

954 **Howell RD, and Pugh JR**. Biphasic modulation of parallel fibre synaptic
955 transmission by co-activation of presynaptic $GABA_A$ and $GABA_B$ receptors in mice. *J*
956 *Physiol* 594: 3651-3666, 2016.

957 **Isope P, Dieudonné S, and Barbour B**. Temporal organization of activity in the
958 cerebellar cortex: a manifesto for synchrony. *Ann N Y Acad Sci* 978: 164-174, 2002.

959 **Ito M**. *The Cerebellum and Neural Control*. New York: Raven Press, 1984.

960 **Jelitai M, Puggioni P, Ishikawa T, Rinaldi A, and Duguid I**. Dendritic excitation-
961 inhibition balance shapes cerebellar output during motor behaviour. *Nat Commun* 7:
962 13722, 2016.

963 **Johansson F, Carlsson HA, Rasmussen A, Yeo CH, and Hesslow G**. Activation of
964 a temporal memory in Purkinje cells by the mGluR7 receptor. *Cell Rep* 13: 1741-
965 1746, 2015.

966 **Jörntell H, Bengtsson F, Schonewille M, and De Zeeuw CI**. Cerebellar molecular
967 layer interneurons - computational properties and roles in learning. *Trends Neurosci*
968 33: 524-532, 2010.

969 **Jörntell H, and Ekerot CF**. Receptive field plasticity profoundly alters the cutaneous
970 parallel fiber synaptic input to cerebellar interneurons in vivo. *J Neurosci* 23: 9620-
971 9631, 2003.

972 **Kaneda M, Wakamori M, Ito C, and Akaike N**. Low-threshold calcium current in
973 isolated Purkinje cell bodies of rat cerebellum. *J Neurophysiol* 63: 1046-1051, 1990.

974 **Katoh A, Shin SL, Kimpo RR, Rinaldi JM, and Raymond JL**. Purkinje cell
975 responses during visually and vestibularly driven smooth eye movements in mice.
976 *Brain Behav* 5: e00310, 2015.

977 **Kekovic G, Stojadinovic G, Martac L, Podgorac J, Sekulic S, and Culic M**.
978 Spectral and fractal measures of cerebellar and cerebral activity in various types of
979 anesthesia. *Acta Neurobiol Exp (Wars)* 70: 67-75, 2010.

980 **Kim J, Lee S, Tsuda S, Zhang X, Asrican B, Gloss B, Feng G, and Augustine GJ**.
981 Optogenetic mapping of cerebellar inhibitory circuitry reveals spatially biased
982 coordination of interneurons via electrical synapses. *Cell Rep* 7: 1601-1613, 2014.

983 **Kondo S, and Marty A**. Synaptic currents at individual connections among stellate
984 cells in rat cerebellar slices. *J Physiol* 509: 221-232, 1998.

985 **Korbo L, Andersen BB, Ladefoged O, and Møller A**. Total numbers of various cell
986 types in rat cerebellar cortex estimated using an unbiased stereological method. *Brain*
987 *Res* 609: 262-268, 1993.

988 **Lemkey-Johnston N, and Larramendi LM**. Types and distribution of synapses
989 upon basket and stellate cells of the mouse cerebellum: an electron microscopic study.
990 *J Comp Neurol* 134: 73-112, 1968.

991 **Lisberger SG**. Internal models of eye movement in the floccular complex of the
992 monkey cerebellum. *Neuroscience* 162: 763-776, 2009.

993 **Liu SJ**. Biphasic modulation of GABA release from stellate cells by glutamatergic
994 receptor subtypes. *J Neurophysiol* 98: 550-556, 2007.

995 **Liu SJ, and Lachamp P**. The activation of excitatory glutamate receptors evokes a
996 long-lasting increase in the release of GABA from cerebellar stellate cells. *J Neurosci*
997 26: 9332-9339, 2006.

998 **Liu Y, Savtchouk I, Acharjee S, and Liu SJ**. Inhibition of Ca^{2+}-activated large-
999 conductance K^+ channel activity alters synaptic AMPA receptor phenotype in mouse
1000 cerebellar stellate cells. *J Neurophysiol* 106: 144-152, 2011.

1001 **Llano I, and Gerschenfeld HM**. Inhibitory synaptic currents in stellate cells of rat
1002 cerebellar slices. *J Physiol* 468: 177-200, 1993.

1003 **Longley M, and Yeo CH**. Distribution of neural plasticity in cerebellum-dependent
1004 motor learning. *Prog Brain Res* 210: 79-101, 2014.

1005 **Maex R, and De Schutter E**. Synchronization of Golgi and granule cell firing in a
1006 detailed network model of the cerebellar granule cell layer. *J Neurophysiol* 80: 2521-
1007 2537, 1998.

1008 **Maex R, and Steuber V**. An integrator circuit in cerebellar cortex. *Eur J Neurosci*
1009 38: 2917-2932, 2013.

1010 **Maex R, Vos BP, and De Schutter E**. Weak common parallel fibre synapses explain
1011 the loose synchrony observed between rat cerebellar golgi cells. *J Physiol* 523 Pt 1:
1012 175-192, 2000.

1013 **Mann-Metzer P, and Yarom Y**. Electrotonic coupling interacts with intrinsic
1014 properties to generate synchronized activity in cerebellar networks of inhibitory
1015 interneurons. *J Neurosci* 19: 3298-3306, 1999.

1016 **Mann-Metzer P, and Yarom Y**. Electrotonic coupling synchronizes interneuron
1017 activity in the cerebellar cortex. *Prog Brain Res* 124: 115-122, 2000.

1018 **Mann-Metzer P, and Yarom Y**. Jittery trains induced by synaptic-like currents in
1019 cerebellar inhibitory interneurons. *J Neurophysiol* 87: 149-156, 2002a.

1020 **Mann-Metzer P, and Yarom Y**. Pre- and postsynaptic inhibition mediated by
1021 $GABA_B$ receptors in cerebellar inhibitory interneurons. *J Neurophysiol* 87: 183-190,
1022 2002b.

1023 **Mathews PJ, Lee KH, Peng Z, Houser CR, and Otis TS**. Effects of climbing fiber
1024 driven inhibition on Purkinje neuron spiking. *J Neurosci* 32: 17988-17997, 2012.
1025 **Mauk MD, and Buonomano DV**. The neural basis of temporal processing. *Annu Rev*
1026 *Neurosci* 27: 307-340, 2004.
1027 **Mejia-Gervacio S, and Marty A**. Control of interneurone firing pattern by axonal
1028 autoreceptors in the juvenile rat cerebellum. *J Physiol* 571: 43-55, 2006.
1029 **Midtgaard J**. Membrane properties and synaptic responses of Golgi cells and stellate
1030 cells in the turtle cerebellum in vitro. *J Physiol* 457: 329-354, 1992.
1031 **Miles FA, Fuller JH, Braitman DJ, and Dow BM**. Long-term adaptive changes in
1032 primate vestibuloocular reflex. III. Electrophysiological observations in flocculus of
1033 normal monkeys. *J Neurophysiol* 43: 1437-1476, 1980.
1034 **Mittmann W, Koch U, and Häusser M**. Feed-forward inhibition shapes the spike
1035 output of cerebellar Purkinje cells. *J Physiol* 563: 369-378, 2005.
1036 **Moczydlowski E, and Latorre R**. Gating kinetics of Ca^{2+}-activated K^{+} channels
1037 from rat muscle incorporated into planar lipid bilayers. Evidence for two voltage-
1038 dependent Ca^{2+} binding reactions. *J Gen Physiol* 82: 511-542, 1983.
1039 **Molineux ML, Fernandez FR, Mehaffey WH, and Turner RW**. A-type and T-type
1040 currents interact to produce a novel spike latency-voltage relationship in cerebellar
1041 stellate cells. *J Neurosci* 25: 10863-10873, 2005.
1042 **Morishita I, and Yajima A**. Analysis and simulation of networks of mutually
1043 inhibiting neurons. *Kybernetik* 11: 154-165, 1972.
1044 **Novikov E, Novikov A, Shannahoff-Khalsa D, Schwartz B, and Wright J**. Scale-
1045 similar activity in the brain. *Phys Rev E* 56: R2387, 1997.
1046 **Nusser Z, Cull-Candy S, and Farrant M**. Differences in synaptic $GABA_A$ receptor
1047 number underlie variation in GABA mini amplitude. *Neuron* 19: 697-709, 1997.

1048 **Ozden I, Dombeck DA, Hoogland TM, Tank DW, and Wang SS**. Widespread
1049 state-dependent shifts in cerebellar activity in locomoting mice. *PLoS One* 7: e42650,
1050 2012.

1051 **Palkovits M, Magyar P, and Szentágothai J**. Quantitative histological analysis of
1052 the cerebellar cortex in the cat. 3. Structural organization of the molecular layer. *Brain*
1053 *Res* 34: 1-18, 1971.

1054 **Pouzat C, and Hestrin S**. Developmental regulation of basket/stellate cell-->Purkinje
1055 cell synapses in the cerebellum. *J Neurosci* 17: 9104-9112, 1997.

1056 **Pouzat C, and Marty A**. Autaptic inhibitory currents recorded from interneurones in
1057 rat cerebellar slices. *J Physiol* 509: 777-783, 1998.

1058 **Pouzat C, and Marty A**. Somatic recording of GABAergic autoreceptor current in
1059 cerebellar stellate and basket cells. *J Neurosci* 19: 1675-1690, 1999.

1060 **Press W, Flannery B, Teukolsky S, and Vetterling W**. *Numerical Recipes in C: the*
1061 *art of scientific computing*. New York: Cambridge University Press 1992.

1062 **Pulido C, Trigo FF, Llano I, and Marty A**. Vesicular release statistics and unitary
1063 postsynaptic current at single GABAergic synapses. *Neuron* 85: 159-172, 2015.

1064 **Rieubland S, Roth A, and Häusser M**. Structured connectivity in cerebellar
1065 inhibitory networks. *Neuron* 81: 913-929, 2014.

1066 **Rigby M, Cull-Candy SG, and Farrant M**. Transmembrane AMPAR regulatory
1067 protein γ-2 is required for the modulation of GABA release by presynaptic AMPARs.
1068 *J Neurosci* 35: 4203-4214, 2015.

1069 **Rossi B, Ogden D, Llano I, Tan YP, Marty A, and Collin T**. Current and calcium
1070 responses to local activation of axonal NMDA receptors in developing cerebellar
1071 molecular layer interneurons. *PLoS One* 7: e39983, 2012.

1072 **Ruigrok TJ, Hensbroek RA, and Simpson JI**. Spontaneous activity signatures of
1073 morphologically identified interneurons in the vestibulocerebellum. *J Neurosci* 31:
1074 712-724, 2011.
1075 **Soler-Llavina GJ, and Sabatini BL**. Synapse-specific plasticity and
1076 compartmentalized signaling in cerebellar stellate cells. *Nat Neurosci* 9: 798-806,
1077 2006.
1078 **Stell BM**. Biphasic action of axonal GABA-A receptors on presynaptic calcium
1079 influx. *J Neurophysiol* 105: 2931-2936, 2011.
1080 **Sullivan MR, Nimmerjahn A, Sarkisov DV, Helmchen F, and Wang SS**. In vivo
1081 calcium imaging of circuit activity in cerebellar cortex. *J Neurophysiol* 94: 1636-
1082 1644, 2005.
1083 **Sultan F**. Distribution of mossy fibre rosettes in the cerebellum of cat and mice:
1084 evidence for a parasagittal organization at the single fibre level. *Eur J Neurosci* 13:
1085 2123-2130, 2001.
1086 **Sultan F, and Bower JM**. Quantitative Golgi study of the rat cerebellar molecular
1087 layer interneurons using principal component analysis. *J Comp Neurol* 393: 353-373,
1088 1998.
1089 **Szapiro G, and Barbour B**. Multiple climbing fibers signal to molecular layer
1090 interneurons exclusively via glutamate spillover. *Nat Neurosci* 10: 735-742, 2007.
1091 **ten Brinke MM, Boele HJ, Spanke JK, Potters JW, Kornysheva K, Wulff P,**
1092 **IJpelaar AC, Koekkoek SK, and De Zeeuw CI**. Evolving models of Pavlovian
1093 conditioning: cerebellar cortical dynamics in awake behaving mice. *Cell Rep* 13:
1094 1977-1988, 2015.

1095 **Tran-Van-Minh A, Abrahamsson T, Cathala L, and DiGregorio DA**. Differential
1096 dendritic integration of synaptic potentials and calcium in cerebellar interneurons.
1097 *Neuron* 91: 837-850, 2016.

1098 **van der Giessen RS, Maxeiner S, French PJ, Willecke K, and De Zeeuw CI**.
1099 Spatiotemporal distribution of connexin45 in the olivocerebellar system. *J Comp*
1100 *Neurol* 495: 173-184, 2006.

1101 **van Welie I, Roth A, Ho SS, Komai S, and Hausser M**. Conditional Spike
1102 Transmission Mediated by Electrical Coupling Ensures Millisecond Precision-
1103 Correlated Activity among Interneurons In Vivo. *Neuron* 90: 810-823, 2016.

1104 **Vervaeke K, Lőrincz A, Gleeson P, Farinella M, Nusser Z, and Silver RA**. Rapid
1105 desynchronization of an electrically coupled interneuron network with sparse
1106 excitatory synaptic input. *Neuron* 67: 435-451, 2010.

1107 **Vicini S, Ferguson C, Prybylowski K, Kralic J, Morrow AL, and Homanics GE**.
1108 $GABA_A$ receptor α1 subunit deletion prevents developmental changes of inhibitory
1109 synaptic currents in cerebellar neurons. *J Neurosci* 21: 3009-3016, 2001.

1110 **Wilms CD, and Häusser M**. Reading out a spatiotemporal population code by
1111 imaging neighbouring parallel fibre axons *in vivo*. *Nat Commun* 6: 6464, 2015.

1112 **Witter L, and De Zeeuw CI**. In vivo differences in inputs and spiking between
1113 neurons in lobules VI/VII of neocerebellum and lobule X of archaeocerebellum.
1114 *Cerebellum* 14: 506-515, 2015.

1115 **Witter L, Rudolph S, Pressler RT, Lahlaf SI, and Regehr WG**. Purkinje cell
1116 collaterals enable output signals from the cerebellar cortex to feed back to Purkinje
1117 cells and interneurons. *Neuron* 91: 312-319, 2016.

1118 **Wulff P, Schonewille M, Renzi M, Viltono L, Sassoe-Pognetto M, Badura A, Gao**
1119 **Z, Hoebeek FE, van Dorp S, Wisden W, Farrant M, and De Zeeuw CI**. Synaptic

1120 inhibition of Purkinje cells mediates consolidation of vestibulo-cerebellar motor
1121 learning. *Nat Neurosci* 12: 1042-1049, 2009.

1122 **Zampini V, Liu JK, Diana MA, Maldonado PP, Brunel N, and Dieudonné S**.
1123 Mechanisms and functional roles of glutamatergic synapse diversity in a cerebellar
1124 circuit. *Elife* 5: 2016.

1125 **Zorrilla de San Martin J, Jalil A, and Trigo FF**. Impact of single-site axonal
1126 GABAergic synaptic events on cerebellar interneuron activity. *J Gen Physiol* 146:
1127 477-493, 2015.

1128

1129

1130 **Figure Captions**

1131

1132 FIG. 1. Temporal integration in a pair of reciprocally coupled inhibitory neurons (after
1133 Cannon et al. (1983)). Two neurons were modeled as half-wave rectified leaky
1134 integrators ($\tau dV_i / dt = -V_i - w\left[V_j\right] + I \pm \Delta I$) inhibiting each other with weight *w*. They
1135 received a shared input *I* between 20 and 80 s, on which a push-pull input ±*ΔI* from
1136 40 to 60 s was superimposed (see inputs in left upper panel). As *w* was varied from
1137 0.9 to 0.999, the time-constant of the response to the push-pull input increased from
1138 the neurons' intrinsic time-constant of 20 ms to 200 ms (*w* 0.9), 2 s (*w* 0.99) and 20 s
1139 (*w* 0.999). Meanwhile the response to the shared input remained fast (actually its
1140 time-constant decreased from 20 ms to ~ 10 ms). Because the neurons would also
1141 amplify the push-pull inputs during the integration process, *ΔI* had to be varied as
1142 well (*ΔI* / *I* = 0.02 for *w* = 0.9, and 0.002 for *w* = 0.99 and 0.999).

1143

1144 FIG. 2. Interneuron model (*A*) and its responses to electrical (*B-D*) and synaptic (*E-G*)
1145 stimulation. *A*: MLI neuron model, with active soma and 21 passive dendritic
1146 compartments. The axon was not modeled explicitly. Black dots in secondary and
1147 tertiary dendritic compartments indicate positions of electrical synapses. *B,C*: voltage
1148 responses to the injection of 10 pA hyperpolarizing current into MLI 233, which was
1149 either isolated (*B*) or electrically coupled in the circuit (*C*). The isolated MLI in *B* and
1150 the entire 800-MLI circuit in *C* were kept subthreshold at -66.4 mV by having E_{leak} set
1151 at -65 mV. MLI 238 (right) was coupled to MLI 233 by two 200-pS gap junctions. *D*:
1152 rebound spiking in an isolated MLI from three different holding potentials. Arrow
1153 lengths indicate first-spike latency. Unequal spike heights are a sampling artifact. *E*:
1154 soma IPSPs after activation of $GABA_AR$ synapses on the soma, or a primary (dend1),

1155 secondary (dend2) or tertiary (dend3) dendritic compartment, for both isolated MLIs
1156 (black traces) and MLIs embedded in a circuit (grey). *F* and *G*: traces of the somatic
1157 membrane potential (*F*) and the $GABA_A$R-generated current (*G*) for MLI 447 during
1158 the first cycle of a sinusoidal PF stimulation protocol. In *G*, MLI 447 had its soma
1159 voltage-clamped at -50 mV and its PF input blocked; resting and junctional currents
1160 were subtracted.
1161
1162 FIG. 3. The MLI circuit and its connection kernels. For visualization, the circuit is
1163 projected on a sagittal (*A*) or frontal plane (*B*). Open circles and filled diamonds in the
1164 bottom panels indicate the positions of the somata of MLIs with caudally and rostrally
1165 projecting axons, respectively. In *A* only half of the length of the circuit is shown. The
1166 upper panels, vertically offset for clarity, show MLI 212 with the skeleton of its
1167 dendrite and the 51 boutons (synapses) on its virtual axon; its soma is located at the
1168 black circle in the bottom raster. Note that the circuit was constructed by first
1169 positioning the somata at the vertices of a regular hexagonal grid and then shifting
1170 randomly their positions, along each of the three dimensions, over distances of
1171 maximally half the grid edge. The connectivity kernel generating the axonal boutons
1172 consisted of two Gaussian ellipsoids positioned at 40 and 160 μm from the soma, and
1173 with semi-axes measuring (60, 60, 60) μm and (40, 100, 60) μm along the (PF,
1174 sagittal, radial) dimensions. The proximal and distal kernels had relative connection
1175 probabilities of 0.5 and 1.5, respectively.
1176
1177 FIG. 4. Responses of the interneuron circuit to sine-wave stimulation of a narrow PF
1178 beam.

1179 *A:* rasterplot of spikes fired over 10 stimulus cycles by the subpopulation of 400 MLIs
1180 with caudally projecting axons. The almost indistinguishable rasterplot of the 400
1181 rostrally projecting MLIs is not shown for clarity. The MLIs are ranked vertically by
1182 their position along the sagittal axis. *B*: spike-rate time-histograms of the PF beam
1183 (averaged over its 141 constituent PFs) and of subpopulations of 20 ON-beam MLIs
1184 (receiving monosynaptic excitation, positioned at black rectangle in *A*) and 20 OFF-
1185 beam MLIs (receiving di-synaptic inhibition, grey rectangle). *C*: histograms averaged
1186 over 100 cycles of the 2048-ms period. Bin-width 16 ms in *B* and *C*. *D*: polar
1187 response plot for each of the 20 ON-beam and 20 OFF-beam MLIs from *B* and *C*.
1188 Response amplitude is distance to the origin (as spike rate). Response phase is the
1189 angle of rotation with respect to the PF input located on the vertical axis (black
1190 diamond). Counter-clockwise rotation indicates phase lag. Black squares are average
1191 vectors. *E*: polar responses for the entire population of 800 MLIs. Grey square is the
1192 average population vector after rectification (see Methods). Axes in *D* and *E* measure
1193 spike rate (s^{-1}).
1194
1195 FIG. 5. Integration times and spiking dynamics vary with the strength of inhibition. *A*:
1196 response amplitude (solid lines, left vertical axis), and response phase expressed as
1197 integration time (broken lines, right axis), calculated from the polar responses of the
1198 same subpopulations of 20 ON-beam (open symbols) and 20 OFF-beam MLIs (closed
1199 symbols) as illustrated in Fig. 4, *B*-*D*, but for varying strengths of inhibition in the
1200 circuit. *B*: mean spike rate ± standard deviation (solid line, left axis) and CV2 of the
1201 interspike interval (broken line, right axis) averaged across all 800 MLIs. *C*: effect of
1202 varying the level of PF excitation. Each graph plots the mean integration time over the
1203 entire circuit (calculated from the population vector, see grey square in Fig. 4*E*) for a

1204 different PF spike rate (increasing from left to right as indicated in the upper legend).
1205 The resulting MLI spike rate is plotted on the horizontal axis. Within each graph the
1206 level of inhibition was varied so as to assess its optimal value, which measured about
1207 100 % (PF rate > 40 s^{-1}), 80 % (40 s^{-1} PF rate), 66 % (10 to 25 s^{-1}), or 400 % (2 and 5
1208 s^{-1}).
1209
1210 FIG. 6. The integration time critically depends on the connection distance (*A*), but not
1211 on the fraction of autapses (*B*) or the circuit length (*C*). *A*: each data point plots the
1212 integration-time of a different MLI circuit as measured from the anti-clockwise
1213 rotation of its population vector (as in Fig. 4*E*). The connection distance (horizontal
1214 axis) was measured as the average sagittal distance between the soma of the afferent
1215 MLI and the postsynaptic compartment of the efferent MLI, averaged over all MLI-
1216 MLI connections in the circuit. Different instantiations of the circuit were generated
1217 by varying either the spacing of MLIs, the connection kernel, the connection
1218 probability, or the strength of inhibition. Black data points are from circuits of MLIs
1219 lacking the CaT channel (see Methods); triangles denote circuits with 40 μm instead
1220 of 20 μm inter-MLI spacing. The grey circle represents the standard version of the
1221 circuit model. Diamond and horizontal line give mean, and standard deviation of the
1222 mean, across sample of 26 MLIs in Sultan and Bower (1998). The insets show the
1223 dendritic trees and axonal boutons of representative caudally and rostrally projecting
1224 MLIs in circuits with mean connection lengths of 40 μm and 131 μm, respectively.
1225 The corresponding connection kernels were as described in the caption to Fig. 2,
1226 except that both kernels were centered at 40 μm for the MLI with the shorter
1227 connection distance. *B*: same data points as in *A* plotted against the fraction of MLIs
1228 making autapses. *C*: Polar responses of a circuit of 1600 MLIs of twice the sagittal

1229 length of the standard circuit. For clarity, MLI responses were lumped into 80 groups
1230 of 20 MLIs. The sinusoidal stimulus was conveyed by three PF beams 400 μm apart.
1231 The PF spike rate was 40 s^{-1} and the strength of inhibition 80 % (which were about
1232 the optimal parameter values according to Fig. 5*C*). Oblique lines of constant phase
1233 are labeled by the corresponding integration time-constants in seconds. Grey square
1234 indicates population average after rectification. Axes have units of spike rate (s^{-1}).
1235

1236 FIG. 7. Pulse stimulation of a PF beam produces slow OFF-beam inhibition. The
1237 stimulus was a 50-ms jump in PF spike rate (from 10 to 500 s^{-1}) of a narrow PF beam
1238 (see Methods). Response histograms in left column plot average spike rate over 20
1239 MLIs located either close to the center of the beam (*a*), or at sagittal distances of 173
1240 and 311 μm (*b* and *c*) (bin-width 10 ms; average of 200 trials). Histograms in right
1241 column were normalized over the mean spike rate during the 200-ms pre-stimulus
1242 interval. The circuit had either full-blown inhibition (100 %), or inhibition reduced to
1243 20 or 10 % as indicated in the legend. Relaxation time in the bottom graph was
1244 calculated as the interval to 1/*e* recovery; negative relaxation times indicate recovery
1245 from troughs.
1246

1247 FIG. 8. Electrical synapses enhance the integration time but have no effect on
1248 synchronization. *A*: Simulations of the same circuit as in Fig. 4 but in the absence of a
1249 PF beam: all PFs fired at a stationary Poisson rate of 10 s^{-1}. Data points plot the time-
1250 constant and modulation depth of the autocorrelogram for each of 40 subpopulations
1251 of 20 MLIs. Inset shows one-sided autocorrelograms (bin-width 1 ms) for four labeled
1252 subpopulations (grey traces) along with their best fitting exponentials (black).
1253 Modulation depth was calculated as percentage peak height above baseline (arrow).

Central peaks in inset are truncated. The lower panel plots the same data for the electrically uncoupled circuit. *B*: Comparison of synchronization in the coupled (left) and uncoupled circuit (right). The spike trains from the subpopulation of 20 MLIs labeled *a* in panel *A* were cross-correlated either among each other (black trace) or with MLIs on average 35 and 70 μm apart (gray). *C*: Details of electrical transmission. An action potential (evoked in MLI 233) spreads to MLIs 238 and 258 via mono- and di-synaptic electrical connections (black traces). Same circuit organization as for Fig. 2*B*, with all MLIs held subthreshold at -61 mV.

FIG. 9. Spectral analysis of spike trains reveals *1/f* scaling at low frequencies. Analysis of the circuit of Fig. 8*A*, with either full-strength inhibition (*A*-*C*), or inhibition of varying strengths compared (*D*-*F*). Power spectra were calculated from the spike-train histograms collected for each of the 40 subpopulations of 20 MLIs, using bin-widths of 1 ms and Hann filtering in sliding windows of 4096 ms length. *A* and *D*: population data of the power-law exponent versus mean spike rate. Vertical axis plots exponent of best-fitting power function within the 0.5-15 Hz domain (the slope of the straight lines in *C* and *F*). *B* and *E*: log-log spectrograms (in arbitrary units) for subpopulations labeled *a*-*d* (*B*) and for subpopulation *c* at varying levels of inhibition (*E*). *C* and *F*: log-log spectrograms from *B* and *E* restricted to the low-frequency domain (grey) with fitted power functions (black). In *C* and *F* traces are offset for clarity.

FIG. 10. Various response types of model PCs receiving PF excitation and MLI inhibition. The model PC had a reduced dendritic tree with an average of 227 PF and 152 MLI synapses. *A*: responses to a 50-ms PF pulse as in Fig. 7. Truncated PF-pulse

1279 peaks at 150 spikes s^{-1}. *B*: phase-lagged responses of the same PCs to 0.25 Hz sine-
1280 wave modulation of the PF beam. *C*: diagram explaining how vector summation of
1281 the PF input (grey arrow on vertical axis) and the OFF-beam MLI response (grey
1282 arrow to lower right quadrant) may generate a PC response that leads the PFs. *D*:
1283 Phase-leading responses of two model PCs receiving twice the strength of PF input.
1284 PC responses averaged over 800 (*A*) or 200 trials (*B* and *D*).
1285

1286

1287 **Tables**

1288

1289 TABLE 1. Characteristics of the $GABA_A$ receptor synapse. IPSCs were calculated
1290 during voltage clamp of the MLI soma at -50 mV, IPSPs from a holding potential of -
1291 60.4 mV. Synapses were activated either on the soma or on primary (dend1),
1292 secondary (dend2) or tertiary (dend3) dendritic branches.

1293

			isolated MLI				circuit MLI			
		conductance	IPSC	IPSP			IPSC	IPSP		
Location	synapses (%)	peak (nS)	peak (pA)	peak (mV)	peak (ms)	1/e decay (ms)	peak (pA)	peak (mV)	peak (ms)	1/e decay (ms)
soma	7.7	2.77	55.5	3.6	5.4	26.6	55.5	3.1	3.5	11.8
dend1	20.4	2.77	26.3	3.1	6.6	27.6	20.5	2.1	4.5	12.4
dend2	29.9	2.77	19.6	2.7	7.5	28.0	12.8	1.6	5.2	12.8
dend3	42.0	2.77	15.5	2.4	8.1	28.1	9.4	1.3	5.7	13.1

1294

1295

1296

1297

1298

1299

1300

1301

1302

1303

1304

1305

1306 TABLE 2. Parameter analysis of the MLI circuit model.

Parameter tested		Value in standard circuit	Range studied	Observed effect on circuit integration time
1. $GABA_AR$ synapses among MLIs	peak conductance	2.77 nS	0-11	integration-time increased with the strength of inhibition, but too strong inhibition aborted integration (Figs. 1 and 5*A*)
	number per MLI	39 ± 11	0-198	
	decay time-constant	3 ms	3-9	unimportant within range tested
2. AMPAR synapses made by PFs	peak conductance	1.8 nS		unimportant except through a secondary effect on activity level (see point 8)
	number per MLI	33.2 ± 5.8	33.2-66.3	
3. electrical synapses among MLIs	conductance	200 pS	0-1600	tended to homogenize the circuit with positive effect on integration (see point 7), and introduced slow IPSPs (Fig. 8*C*)
4. MLI parameters	passive dendrite			dendritic filtering was unimportant
	soma channels			model MLI with CaT channels tended to enhance integration
	spike-rate adaptation			being a form of self-inhibition, strong adaptation hampered integration
5. circuit size	MLI number	800	400-2000	unimportant within range tested (see Figs. 6*B*,*C*)
	inter-MLI distance	20 µm	20-40	
6. circuit connectivity	mean distance of axonal boutons	135.2 ± 62	39.8-135.2	should be greater than sagittal width of dendritic tree (86 µm) (Fig. 6*A*)
	autapses			unimportant if present in small numbers (Fig. 6*B*)
7. circuit heterogeneity				lateral inhibition in a too heterogeneous circuit can lead to a winner-takes-all dynamics, precluding integration
8. level of activity	spike rate of afferent PFs	10 Hz	0-100	integration declined only at very low spike rates (Fig. 5*C*)

1307

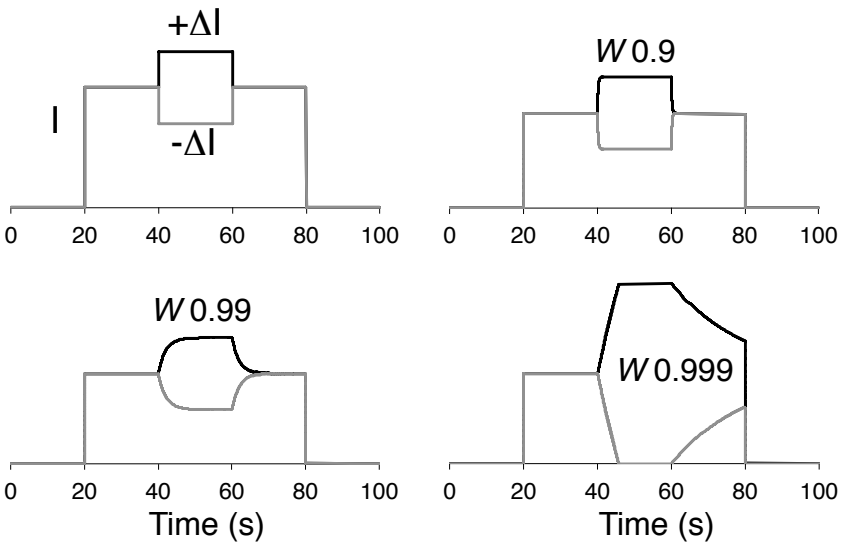

Figure 1

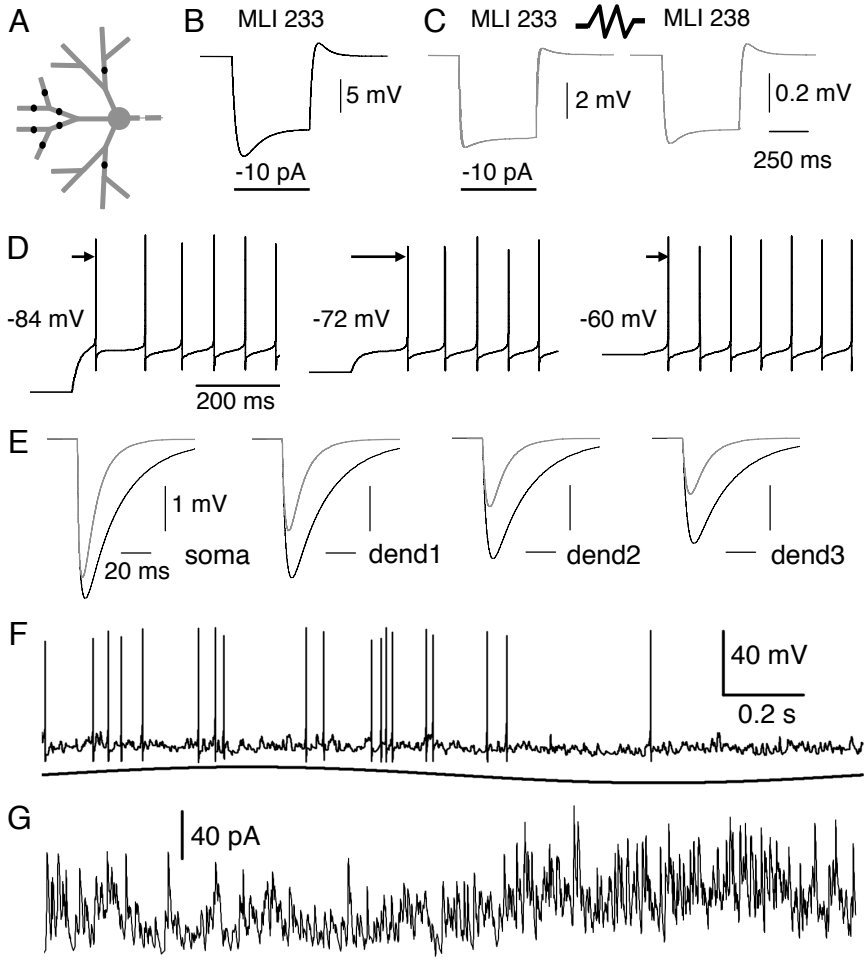
A
B
MLI 233
5 mV
-10 pA
C
MLI 233
MLI 238
2 mV
0.2 mV
-10 pA
250 ms
D
-84 mV
-72 mV
-60 mV
200 ms
E
1 mV
20 ms
soma
dend1
dend2
dend3
F
40 mV
0.2 s
G
40 pA

Figure 2

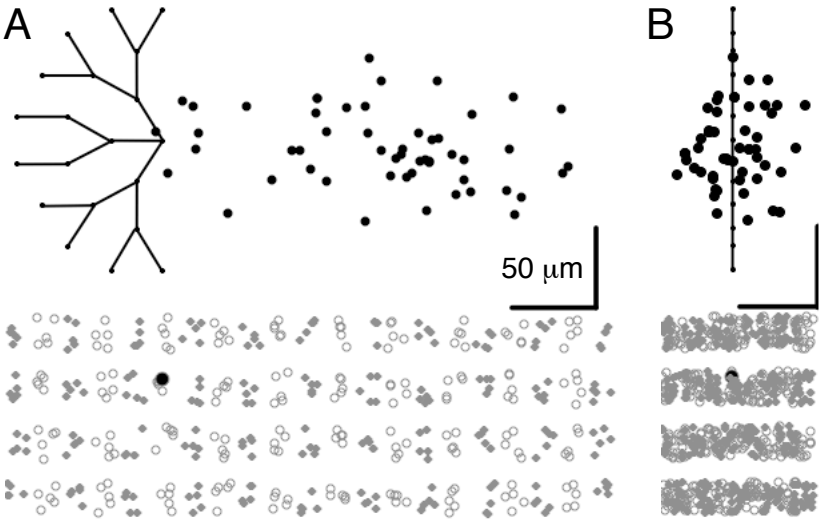

Figure 3

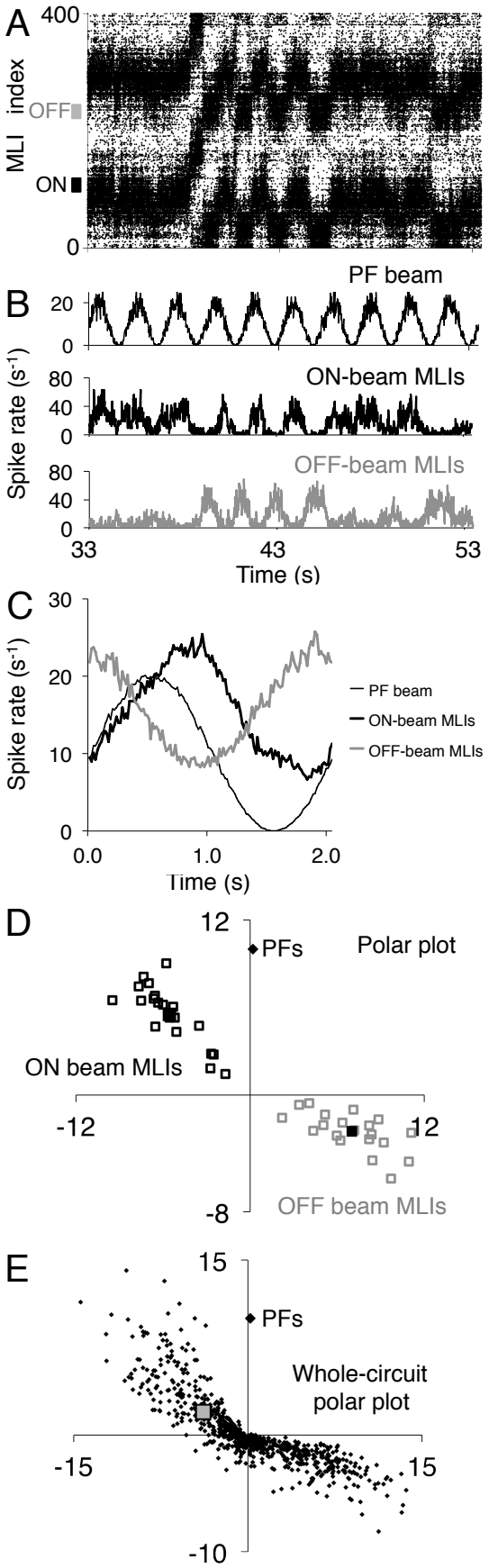
A
400
MLI index
OFF
ON
0
B
PF beam
20
0
Spike rate (s-1)
80
40
0
ON-beam MLIs
80
40
0
OFF-beam MLIs
33
43
53
Time (s)
C
30
20
10
0
Spike rate (s-1)
PF beam
ON-beam MLIs
OFF-beam MLIs
0.0
1.0
2.0
Time (s)
D
12
PFs
Polar plot
ON beam MLIs
-12
12
-8
OFF beam MLIs
E
15
PFs
Whole-circuit
polar plot
-15
15
-10

Figure 4

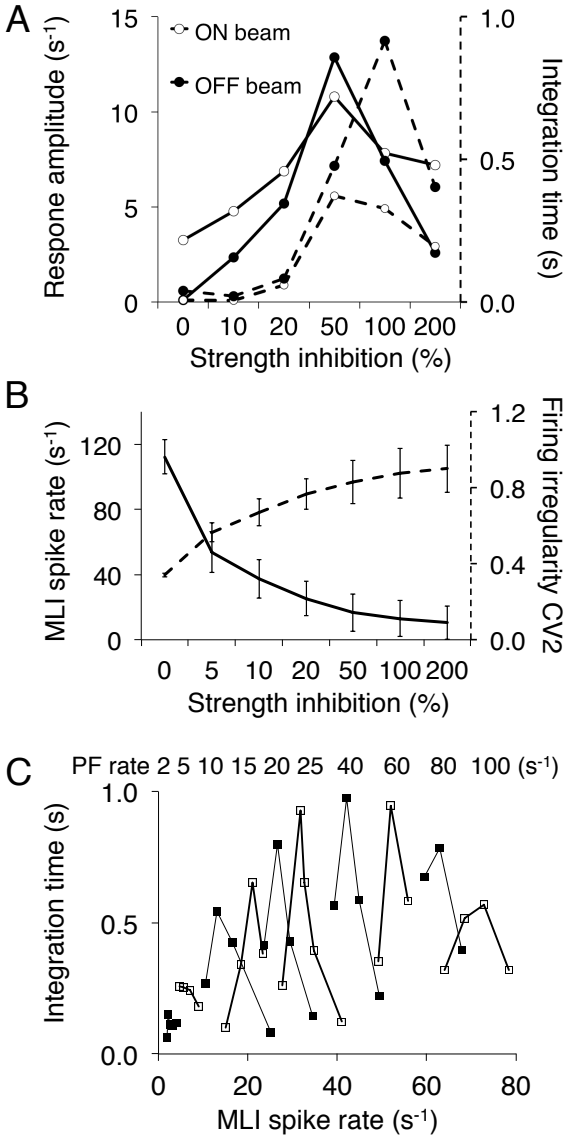
A
ON beam
OFF beam
Respone amplitude (s-1)
Integration time (s)
15
10
5
0
1.0
0.5
0.0
0 10 20 50 100 200
Strength inhibition (%)
B
MLI spike rate (s-1)
Firing irregularity CV2
120
80
40
0
1.2
0.8
0.4
0.0
0 5 10 20 50 100 200
Strength inhibition (%)
C
PF rate 2 5 10 15 20 25 40 60 80 100 (s-1)
Integration time (s)
1.0
0.5
0.0
0 20 40 60 80
MLI spike rate (s-1)

Figure 5

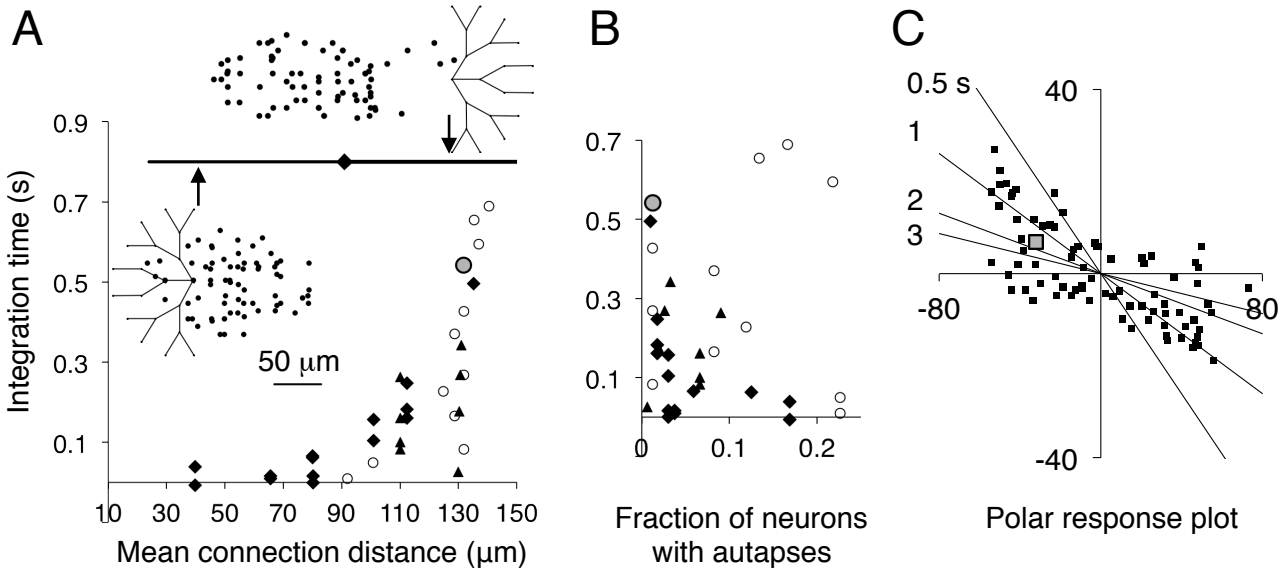
A
B
C
Integration time (s)
0.9
0.7
0.5
0.3
0.1
50 μm
10
30
50
70
90
110
130
150
Mean connection distance (μm)
0.7
0.5
0.3
0.1
0
0.1
0.2
Fraction of neurons
with autapses
0.5 s
1
2
3
40
-40
-80
80
Polar response plot

Figure 6

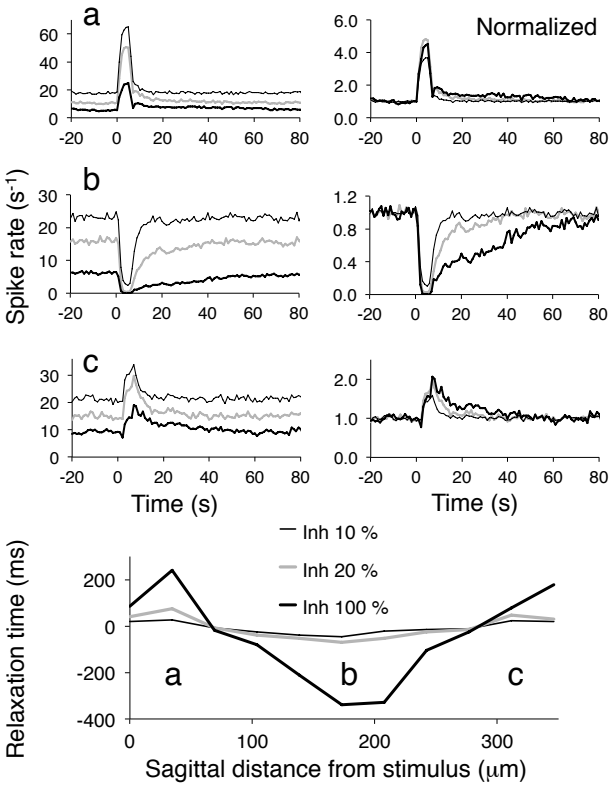
a
b
c
Normalized
Spike rate (s-1)
Time (s)
Time (s)
Inh 10 %
Inh 20 %
Inh 100 %
Relaxation time (ms)
Sagittal distance from stimulus (μm)

Figure 7

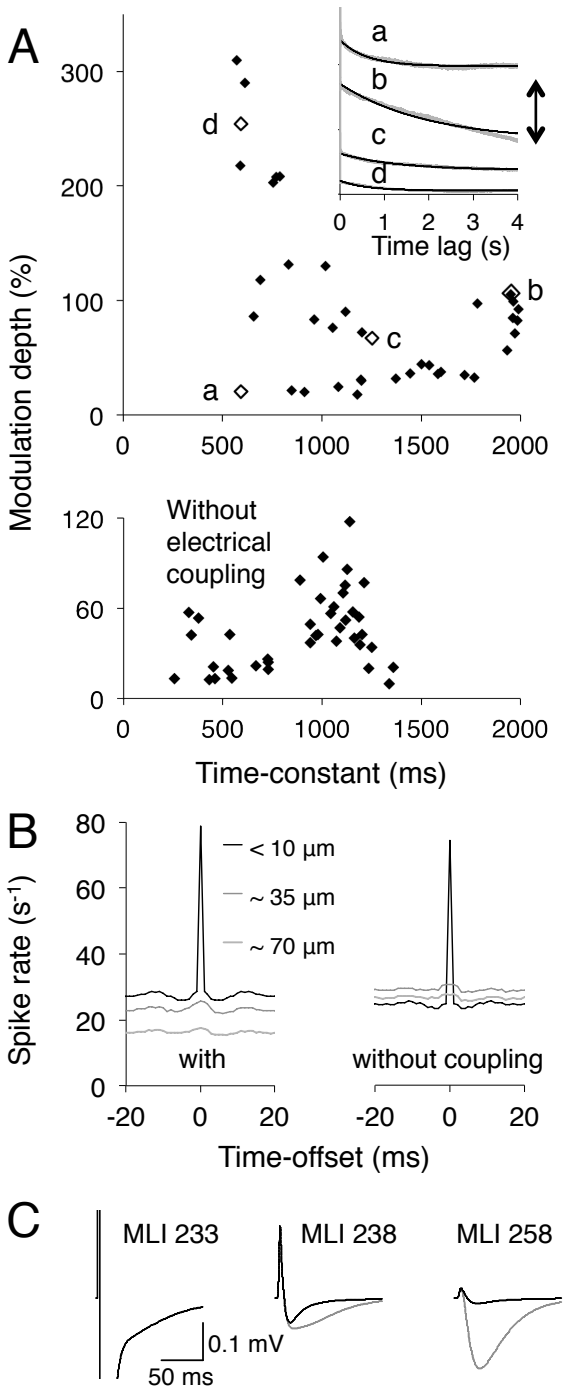
A
Modulation depth (%)
300
200
100
0
0
500
1000
1500
2000
a
b
c
d
0
1
2
3
4
Time lag (s)
Without
electrical
coupling
120
60
0
Time-constant (ms)
B
Spike rate (s-1)
80
60
40
20
0
< 10 µm
~ 35 µm
~ 70 µm
with
without coupling
-20
0
20
Time-offset (ms)
C
MLI 233
MLI 238
MLI 258
0.1 mV
50 ms

Figure 8

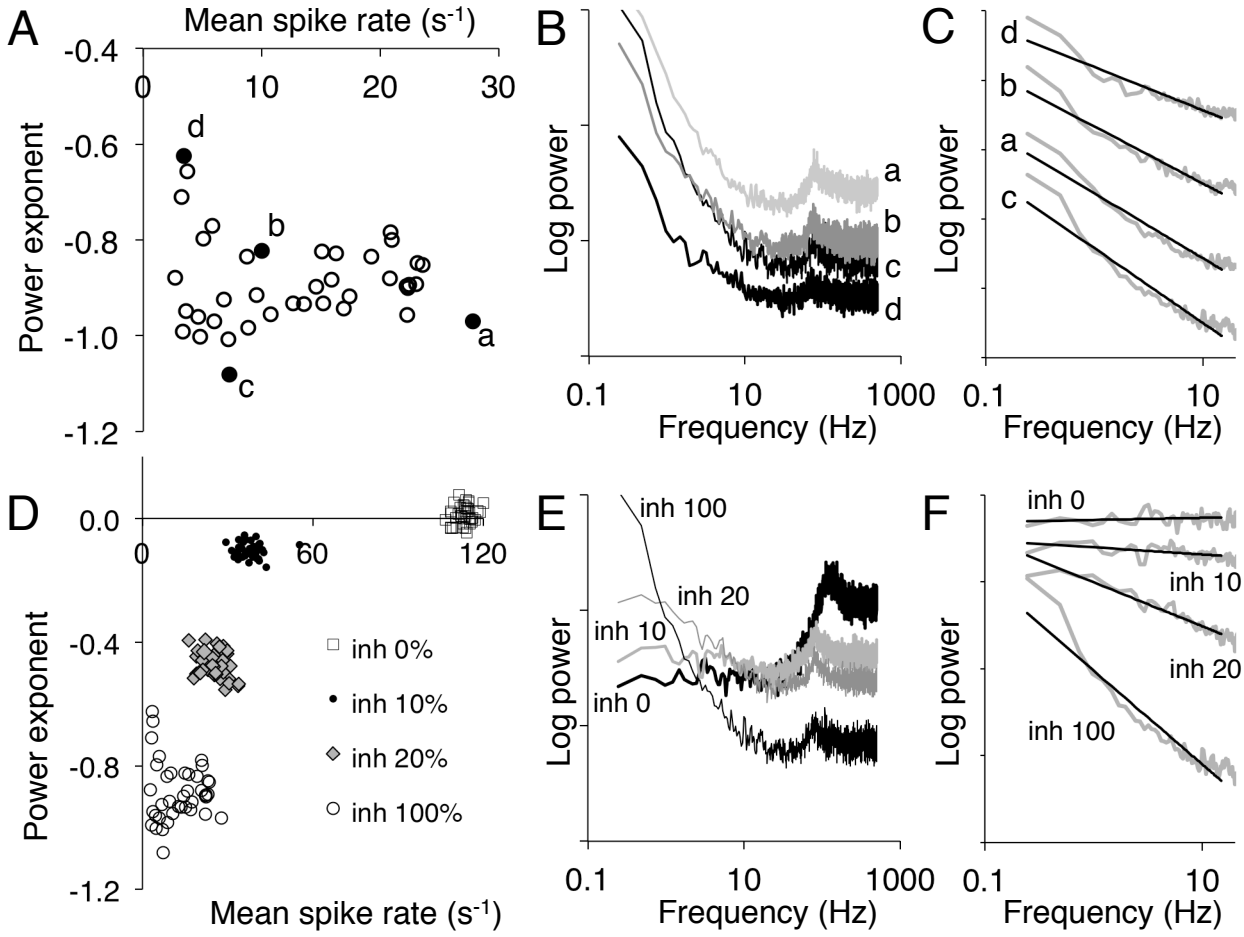
A
Mean spike rate (s-1)
Power exponent
-0.4
-0.6
-0.8
-1.0
-1.2
0
10
20
30
a
b
c
d
B
Log power
Frequency (Hz)
0.1
10
1000
a
b
c
d
C
Log power
Frequency (Hz)
0.1
10
d
b
a
c
D
Power exponent
0.0
-0.4
-0.8
-1.2
0
60
120
inh 0%
inh 10%
inh 20%
inh 100%
Mean spike rate (s-1)
E
Log power
Frequency (Hz)
0.1
10
1000
inh 100
inh 20
inh 10
inh 0
F
Log power
Frequency (Hz)
0.1
10
inh 0
inh 10
inh 20
inh 100

Figure 9

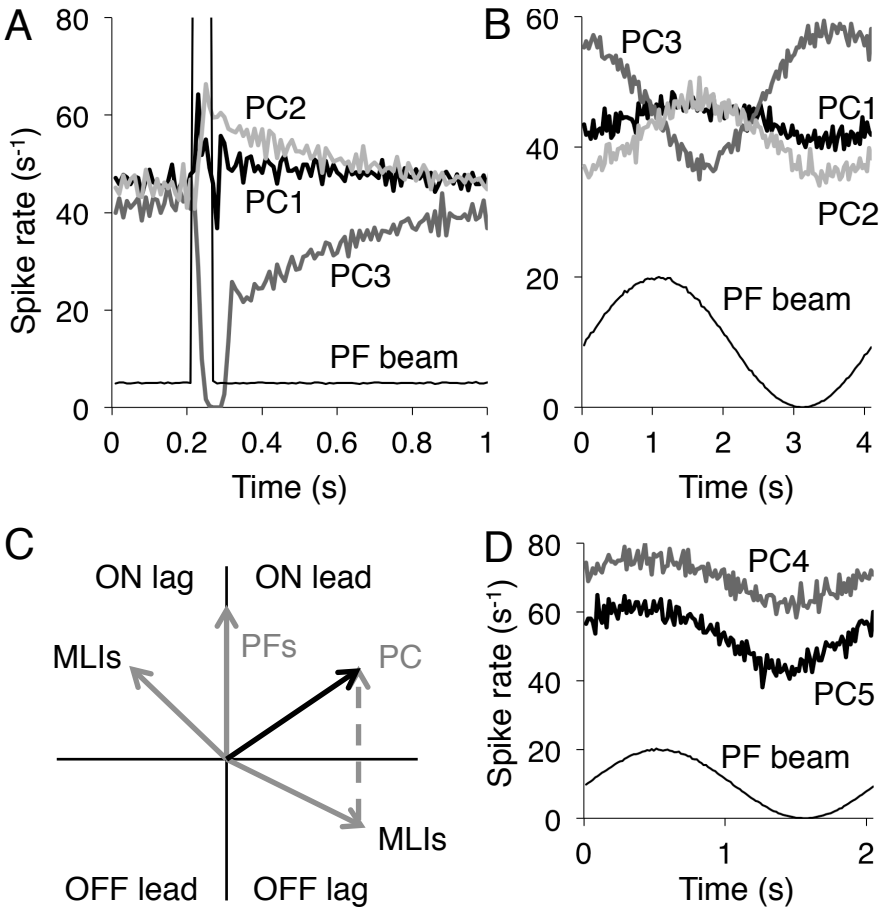
A
80
60
40
20
0
Spike rate (s-1)
PC2
PC1
PC3
PF beam
0
0.2
0.4
0.6
0.8
1
Time (s)
B
60
40
20
0
PC3
PC1
PC2
PF beam
0
1
2
3
4
Time (s)
C
ON lag
ON lead
MLIs
PFs
PC
MLIs
OFF lead
OFF lag
D
80
60
40
20
0
Spike rate (s-1)
PC4
PC5
PF beam
0
1
2
Time (s)

Figure 10